MINISTRY OF EDUCATION AND TRAINING

HANOI UNIVERSITY OF TECHNOLOGY

---------ꕥ♣ꕥ---------

MASTER THESIS

THE CHERENKOV COUNTERS OF THE VATLY LABORATORY

ENGINEERING PHYSICS
CODE: 02.01

PHAM NGOC DONG

SUPERVISOR: Prof. PIERRE DARRIULAT

Hanoi - 2006

Abstract

The present work describes detectors that have been constructed for the detection of cosmic rays at the Vietnam Auger Training LaboratorY (VATLY) in Hanoi. It gives details about their design, their operation and their performance. It concerns both the large Cherenkov counter that is a replica of those used in the surface detector of the Pierre Auger Observatory and three additional smaller counters, also water Cherenkov detectors, which have been installed around it in order to provide a trigger on extensive air showers.

Table of Contents

ACKNOWLEDGEMENTS

First of all, I would like to thank all the members of Vietnam-Auger Training LaboratorY (VATLY) for invaluable support to perform my thesis at Institute for Nuclear Science and Technology. Without them and their contributions I could not have completed this thesis.

I express my deepest gratitude to my supervisor, Professor Pierre Darriulat, who has pushed me whole time. He teaches me not only to do research but also gives me a lot of things to learn in life. He has required so much of me that I have been able to grow as much as I have.

I am particularly grateful to Dr. Vo Van Thuan, Dr. Dang Quang Thieu for tutoring and advice since I became a new member of the group. I also would like to give my thankfulness to young members of VATLY, Pham Ngoc Diep, Pham Thi Tuyet Nhung, Nguyen Thi Thao for their kind friendship and much discussion that I have learnt a lot of things from them.

I wish to thank professors of Institute of Engineering Physics as well as professors of Department of Nuclear Engineering and Environmental Physics for giving lectures and encouragements when I studied at Hanoi University of Technology.

I am also thankful to the Pierre Auger Collaboration for their instant interest and valuable support. I am particularly grateful to Professors Jim Cronin, Murat Boratav, Pierre Billoir, Tiina Suomijärvi, Antonio Insolia, Paul Sommers for their useful lectures and comments, in the work and progress of our group.

I would like to thank the French CNRS, CERN, RIKEN, the Rencontres du Vietnam, the Odon Vallet fellowships, the World Laboratory and the Ministry of Science and Technology for invaluable support.

Finally, I am deeply indebted to my family who always encourages and supports me in my study period.

Preamble

The present work describes detectors that have been constructed for the detection of cosmic rays at the Vietnam Auger Training LaboratorY (VATLY) in Hanoi. It gives details about their design their operation and their performance. The first chapter gives an introduction to cosmic ray research and to the Pierre Auger Observatory (PAO) with which VATLY is closely associated. The second chapter is dedicated to a replica of one of the 1600 counters of the surface detector (SD) of the PAO that has been constructed and operated in Hanoi. The third chapter describes three smaller counters that have been designed and constructed in VATLY with the aim of detecting and studying the response of the main Cherenkov counter to extensive air showers. The emphasis of this thesis work is on instrumental aspects of these detectors to which the author has made essential contributions. The fourth chapter summarizes some results obtained with the complete system while a summary of the present work and perspectives for the future are presented in the conclusion.

Chapter 1

Cosmic ray research and the Pierre Auger Observatory (PAO)

1.1 Introduction to cosmic ray research

1.1.1 A few landmarks in the history of high energy cosmic rays

"Cosmic rays" is the name given to the high energy charged particles which strike the Earth from space.

In 1912, in a balloon at an altitude of 5000 meters, Victor Hess, the founding father of cosmic ray research, discovered penetrating radiation coming from space. This was the first of many adventurous journeys made by physicists to study cosmic rays.

In 1927, Dimitri Skobelzyn used a cloud chamber to photograph the first cosmic ray tracks.

In 1932, while watching the tracks of cosmic ray particles passing through a cloud chamber that he was tuning and running in, Carl Anderson discovered antimatter in the form of the antielectron, later called the positron.

A debate raged over the nature of cosmic rays. According to a theory of Robert Millikan, they were gamma rays from space hence their name. But evidence was mounting that cosmic rays were, in fact, mostly energetic charged particles.

In 1937, Seth Neddermeyer and Carl Anderson discovered the muon in cosmic rays. The positron and the muon were the first of a series of subatomic particles discovered using cosmic rays, discoveries that gave birth to

elementary particle physics. Particle physicists used cosmic rays for their research until the advent of particle accelerators in the 1950s.

In 1938, Pierre Auger, who was running particle detectors high in the Alps and using coincidence circuits, a new technique at the time, noticed that two detectors located several meters apart signaled the arrival of particles at the same time. Auger had discovered extensive air showers of secondary subatomic particles caused by the collision of primary cosmic rays with air molecules. On the basis of his measurements, Auger concluded that he had observed showers with energies of 10^{15} eV, ten million times higher than known before.

Figure 1.1 Pierre Auger, one of the founding father of CERN, UNESCO and the European Space Agency.

In 1946, groups led by Bruno Rossi in the USA and Georgi Zatsepin in Russia started experiments on the structure of Auger showers. These researchers constructed the first arrays of correlated detectors to detect air showers.

In 1949, Enrico Fermi put forth an explanation for the acceleration of cosmic rays. In Fermi's cosmic ray shock accelerator, protons speed up by bouncing off moving magnetic clouds in space. Exploding stars (supernovae) are believed today to act as such cosmic accelerators, but they alone cannot account for the highest energy cosmic rays.

In 1962, John Linsley and collaborators detected the first cosmic ray reaching an energy of about 10^{20} eV in the Volcano Ranch array in New Mexico.

In the early 1960s Arno Penzias and Robert Wilson discovered that low-energy microwaves permeate the universe. Shortly after, Kenneth Greisen, Vadem Kuzmin and Georgi Zatsepin pointed out that high energy cosmic rays would interact with the microwave background [1]. The interaction would reduce their energy, so that particles traveling long intergalactic distances could not have energies greater than 5×10^{19} eV.

In 1991, the Fly's Eye cosmic ray research group in the USA observed a cosmic ray event with energy of 3×10^{20} eV [2]. Events with energies of 10^{20} eV had been reported in the previous 30 years, but this was clearly the most energetic.

In 1994, the AGASA Group in Japan and the Yakutsk group in Russia each reported an event with energy of 2×10^{20} eV [3]. The Fly's Eye event and these events are higher in energy than any seen before. Where did these three high-energy cosmic rays come from? None seemed to point back to an astrophysical object that could impart such enormous energies.

In 1995, an international group of researchers began design studies for a new cosmic ray observatory, the Pierre Auger Observatory (PAO) [4] named in honor of the discoverer of air showers. The new observatory uses a giant array of detectors to detect and measure large numbers of air showers from the very highest-energy cosmic rays which can hopefully be traced back to their unknown sources.

1.1.2 Nature and origin of cosmic rays

The existence of cosmic rays has been known for nearly a century but we still do not understand very well where they come from and how they have been accelerated [5, 6]. The most surprising feature of cosmic rays is that they reach very high energies up to 10^{20}eV, namely 16 Joules! –where so few of them carry so much energy: their flux around 10^{20}eV is only of the order of 1/km^2/sr/century.

For most of the energy range cosmic rays are known to consist of fully ionized atomic nuclei, mostly protons. Their energy density in the universe is of the order of magnitude of 1 eV/cm^3, similar to those of magnetic fields, of visible light and of cosmic microwave background (CMB) photons. Their flux on the Earth spans 32 orders of magnitude and decreases with energy as a power law ~$E^{-2.7}$ on average (Figure 1.2).

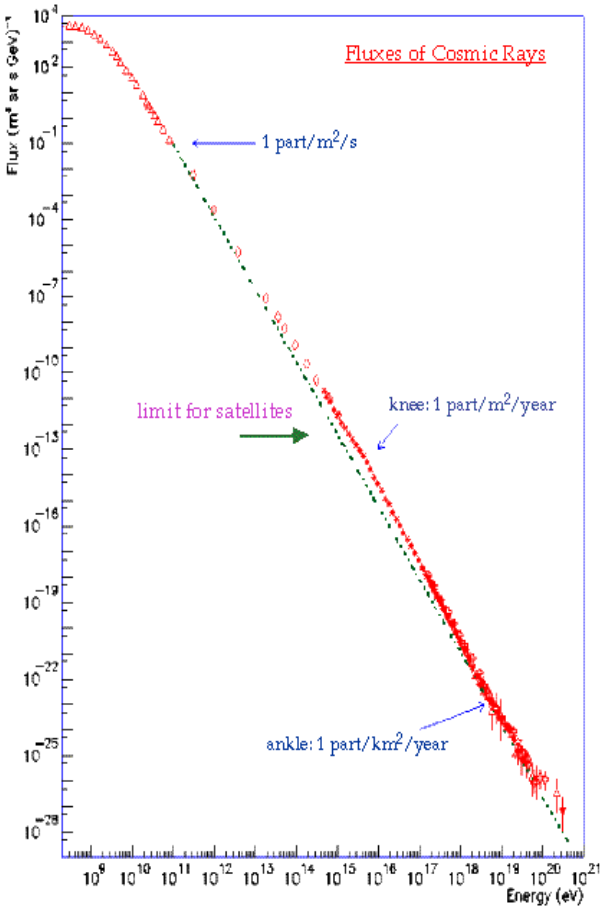

Figure 1.2 : The distribution of the primary cosmic ray flux reaching the earth as a function of energy (eV)

This law is in fact the convolution of the production at the source with the effect of propagation in the interstellar medium. Taking the latter in due account (it takes 10My to a typical cosmic ray to reach the Earth from its source) one finds a spectral index between 2 and 2.5 rather than 2.7. In fact small variations are observed; in particular two

breaks, above 10^{15} and 10^{18} eV respectively, referred to as the “knee” and the “ankle”, have not yet received satisfactory explanations. The abundance of elements present in cosmic rays follows closely that of elements in the universe (Figure 1.3), except for the rarer elements which are present in cosmic rays with a higher abundance. This is explained by the spallation reactions which occur when the cosmic rays interact with interstellar matter. On average they traverse some $7 g/cm^2$ of matter before reaching the Earth.

At low energies their trajectories are strongly bent by the magnetic fields of the Earth and of the solar system in general, that have the effect of shielding the Earth: one speaks of a rigidity cutoff. Similarly, most cosmic rays are trapped into the Milky Way by the magnetic field (~1μG) that pervades it. It is only above 10^{15}eV that one believes that cosmic rays are of mostly extragalactic origin.

The solar wind is known to be a source of low energy cosmic rays modulated by the 22 year solar cycle. Galactic cosmic rays are believed to be produced dominantly in supernova remnants. The galactic magnetic field prevents the identification of precise sources in the sky up to very high energies. But gamma rays are good tracers of high energy cosmic rays: when very high energy nuclei interact with matter present on their path they produce neutral pions (among other mesons) that decay very promptly into a pair of photons. Several sources have been identified this way; they generally consist of a supernova remnant (SNR).

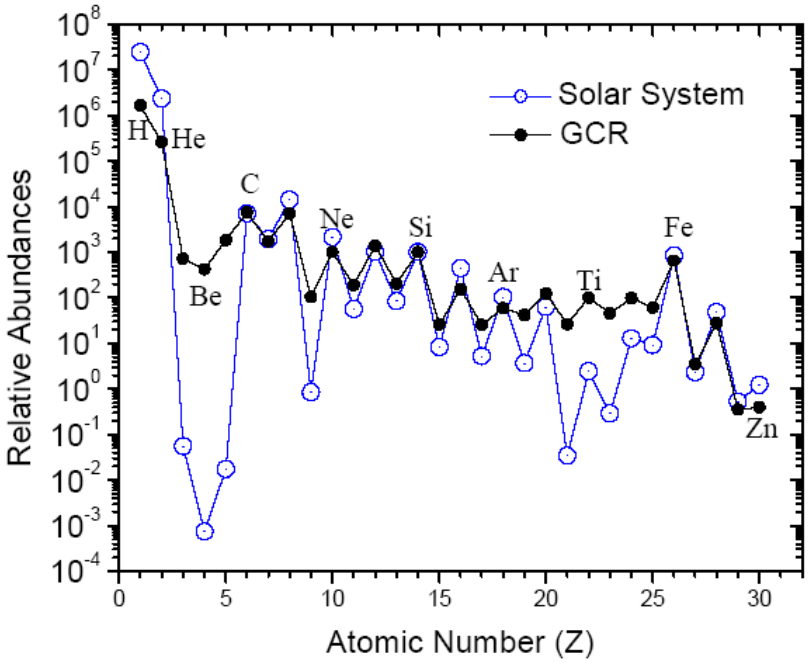

Figure 1.3 The abundance of galactic cosmic rays (full circles). For comparison, the open circles show the abundances of elements in the solar system. The filling of the valleys is understood as being due to spallation reactions.

Extragalactic cosmic rays are more difficult to understand. Because of the extraordinary energy requirement, only violent events, such as Active Galatic Nuclei (AGN)'s or Gamma Ray Bursts (GRB)'s, are plausible candidates [7]. Indeed several AGN's (blazars) have been observed to be sources of very high energy gammas (Figure 1.4). As far as GRB's are concerned one would expect the cosmic ray burst to be delayed with respect to the gamma ray burst by such a long time (several years) that it is hopeless to detect any correlation: over such large distances the intergalactic magnetic fields should significantly lengthen the path of cosmic rays. The most popular models extend the phenomena that are believed to occur in SNR's to the cases of AGN's and GRB's.

However, above an energy of the order of $0.5\ 10^{20}$ eV, the universe is expected to become opaque to cosmic rays over an attenuation length of the

order of 30 Mpc; such energies are above the threshold for photoproduction of pions on the CMB photons, called the Greisen-Zatsepin-Kuzmin (GZK) threshold [1]. It corresponds to the threshold for inelastic collisions between the CMB and protons or heavy nuclei. Consequently, if Ultra High Energy Cosmic Rays (UHECRs, above 10^{18} eV) having energy in excess of 10^{20}eV are observed on Earth and are protons or heavier nuclei, they must be produced in our vicinity (Figure 1.5).

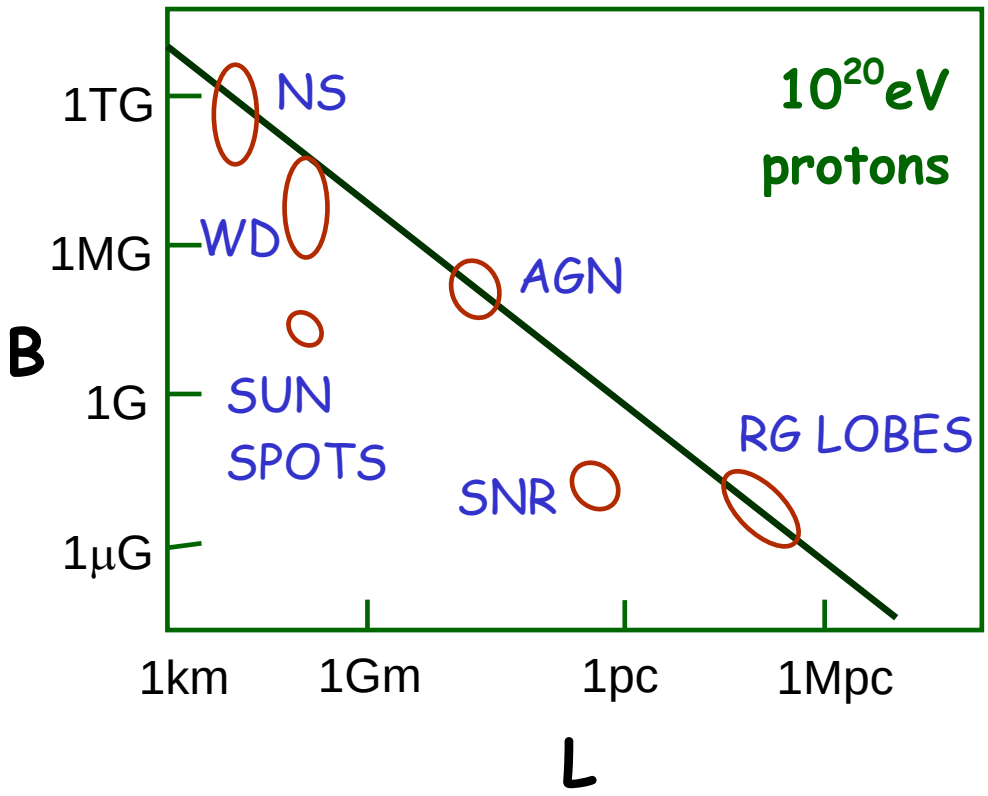

Figure 1.4 Plot showing the minimal value of the product BL (magnetic field × size) for accelerating a proton to 10^{20} eV. The limit is shown as a line in the log-log plot. A few candidate sites are indicated.

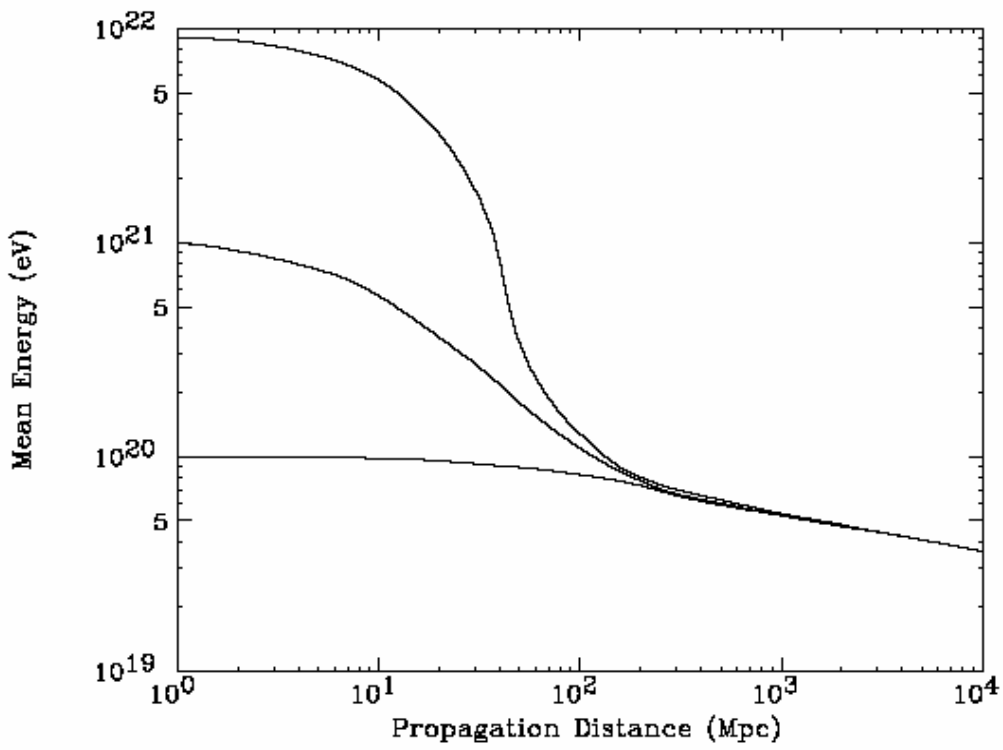

Figure 1.5 Mean energy of protons as a function of propagation distance through CMB. Curves are for energy at the source of 10^{22} eV, 10^{21} eV, 10^{20} eV.

It is a matter of current controversy whether cosmic rays have been or have not been observed beyond this threshold: almost forty years after the GZK publication it is not yet clear if the effect is observed or not. The two largest experiments preceding Auger, AGASA and HiRes have reported inconsistent results. As seen from Figure 1.6 the Auger data [8] will very soon resolve the discrepancy.

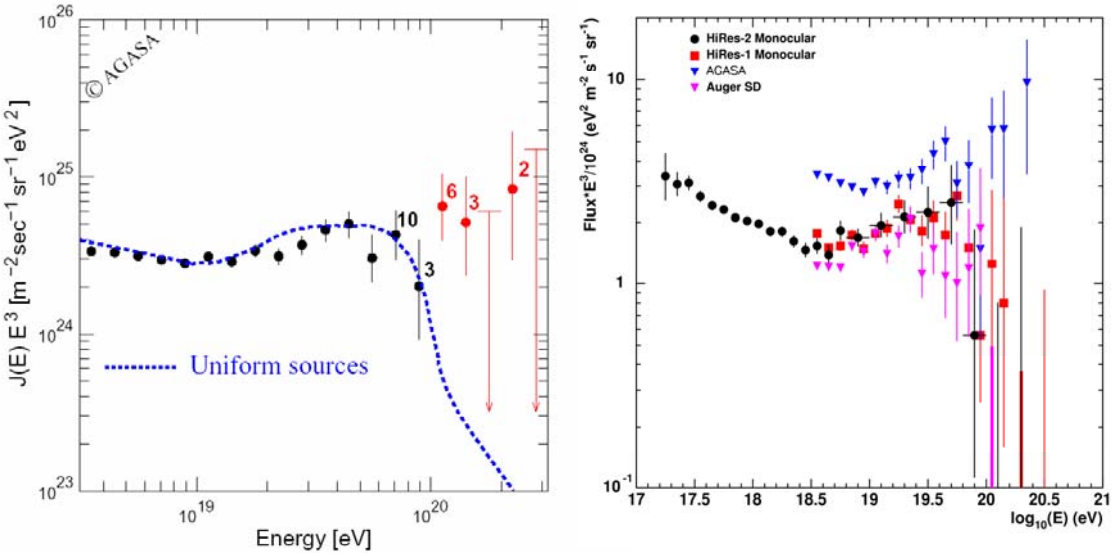

Figure 1.6 a. Left: Differential energy spectrum ($\times E^3$) from the AGASA experiment. The dotted line is the result of a simulation in the region of the GZK cut-off.
Right: Combined differential energy spectra ($\times E^3/10^{24}$) from the HiRes (1 and 2 monocular), AGASA and Auger (SD) experiments.

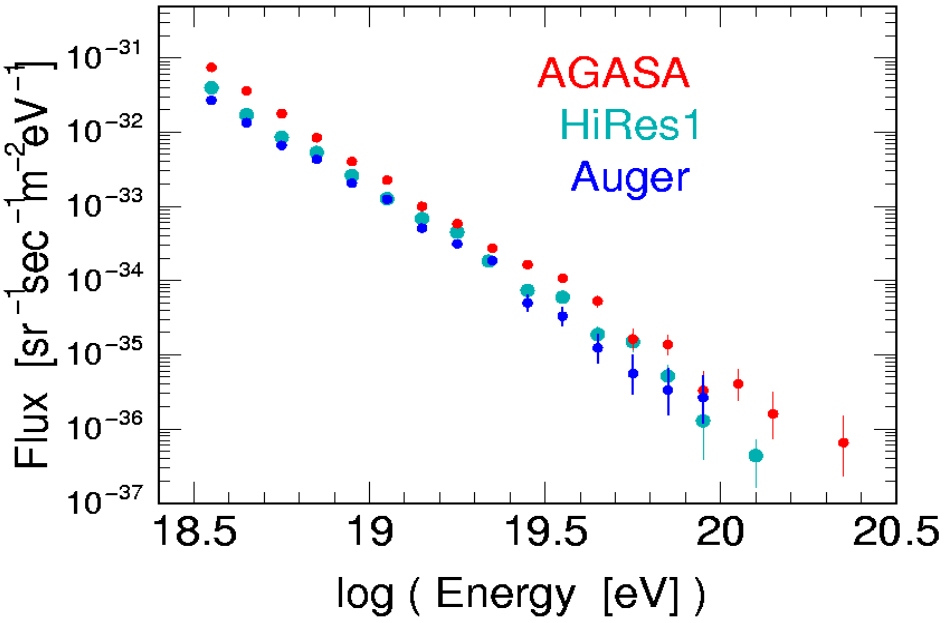

Figure 1.6 b. Differential energy spectra as observed by the HiRes, AGASA and Auger experiments.

1.1.3 Introduction to the PAO

The PAO consists of two giant air shower arrays, one in the southern and one in the northern hemisphere, the latter being in the design stage. The construction of the array in the southern hemisphere is nearly completed. It is located in Argentina at 1400 m altitude and includes a so-called surface detector (SD) made of 1600 water Cherenkov detectors and covering 3000 km^2, and four sets of fluorescence telescopes. The joint use of the two techniques, making the PAO a hybrid detector, is one of its main assets as the systematic uncertainties affecting the two techniques are independent. The PAO detects UHECR's through the extensive air showers that they produce when entering the Earth atmosphere. It measures their energy spectrum, arrival direction, and composition with a large statistics (about one event per week in the GZK region) and good control over systematic uncertainties [9].

The main physics goal of the PAO is an accurate measurement of the high end of the energy spectrum. Above 10^{20} eV or so, as we have seen earlier, one expects the spectrum to be cut off unless UHECR sources are close to us (*ie* are not active galactic nuclei). The hybrid nature of the PAO, combined with its very large area, should settle the currently controversial GZK question unambiguously. The PAO should help identify UHECR sources if, as one believes, the intergalactic magnetic field is not so strong that it would irremediably smear their direction of arrival on Earth. Also, through detailed studies of the extensive air showers produced by UHECRs, the PAO should help pinning down their composition.

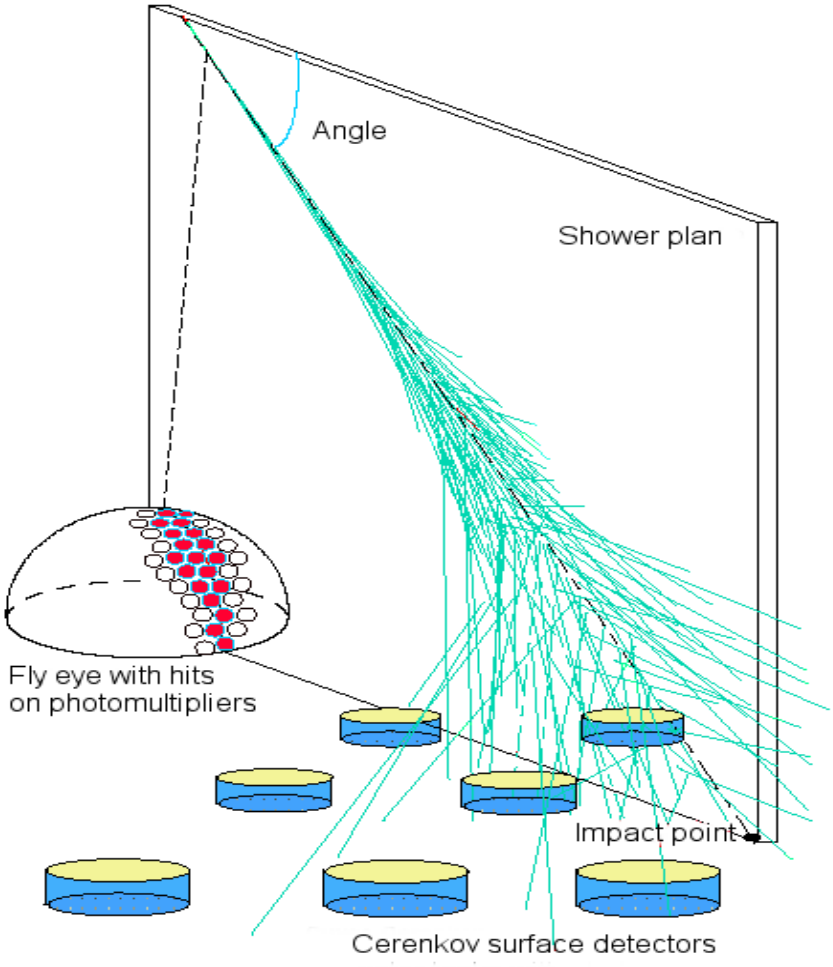

Figure 1.7.: The Pierre Auger Observatory is an hybrid cosmic ray detector under completion in the Argentinean pampas.

For the array alone the energy and angular resolutions are 20% and less than 1^0 respectively. In the hybrid mode, the detector is expected to have on average 10% energy resolution and an angular precision of about $\pm 0.6^o$ [10]. The bending of a 10^{19}eV cosmic ray is expected not to exceed 10^o, which should be sufficient to identify the brightest sources. However, this quantity is difficult to evaluate reliably because little is known of the intergalactic fields.

1.2 The Surface Detector (SD)

1.2.1 Design of the array

The SD (Figure 1.8) consists of about 1600 water Cherenkov counters spaced on a triangular grid with about 1.5 km separation between individual detectors and encompasses an area of 3000 km^2. The construction of the observatory started in 1999 and is expected to be completed in 2007 [4]. By the end of 2006, more than 1100 fully instrumented water tanks and three FD will have been installed and be in operation.

The altitude of the site, ~ 1400 m above sea level, corresponds to an atmospheric depth of some 875 g/cm^2, namely to shower maximum for vertical showers in the energy range of interest.

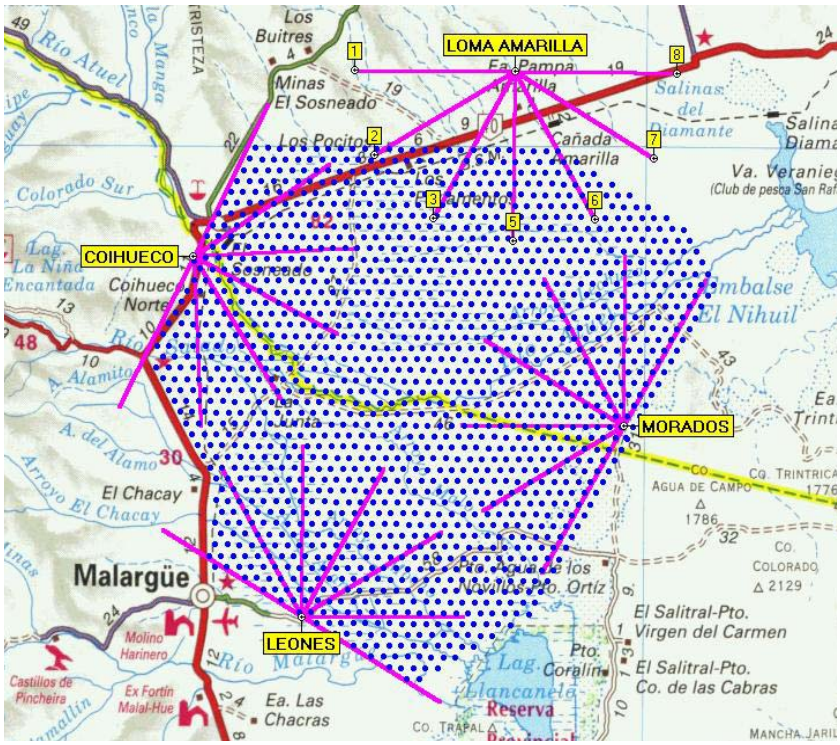

Figure 1.8 Map of the PAO site. Each dot represents the position of a Cherenkov tank. The array is viewed from four sides by fluorescence detectors.

For events having five detector signals above trigger threshold, the array is fully efficient at 10^{19}eV.

1.2.2 The water Cherenkov tanks

The low density of particles (~1/m^2) to be measured with good statistical precision imposes a sampling area of ~10 m^2. The water Cherenkov detection technique has been selected mainly from cost considerations but also because of its own virtues: it offers a good balance between the responses to muons and to the electromagnetic component (electrons and photons). The separation between these two components is a useful tool in the identification of the nature of the primary, however it is nearly impossible on an event to event basis and can only be performed on a statistical basis. Because of its large lateral cross-section (4.3 m^2), the water Cherenkov detector offers a good sensitivity to large zenith angle showers. The experience from the Haverah Park [11] array, where water Cherenkov detectors of similar area and height were used, backs this choice.

Each detector consists of a cylindrical, opaque tank having a diameter of 3.6 m and filled with ultra pure water to a height of 1.2 m. Three large diameter (9") hemispherical photomultipliers (PMTs) are mounted face down on the top of the tank. This allows for a good background rejection and for an easy identification of spurious signals caused by a charged particle crossing the photocathode of one of the PMT's. Ultra high purity water is being used with an attenuation length to the detected Cherenkov wave lengths (350÷420 nm) of the order of 70±30 m [9]. A special purification unit, using in particular resin filters, is installed on the site for this purpose. The water is contained in a sealed bag or liner that prevents contamination and diffusely reflects the Cherenkov light until it escapes to the photocathode of one of the

PMT's through one of the windows sealed on its upper part. The high quality of the diffusing surface, together with that of the water transparency, allow for an excellent light collection, implying six diffusions on average, as can be checked by the long decay time of the PMT signal, 100 ns on average. The liner also provides filling ports and an additional sealed window hosting an LED calibration system. The PMTs are enclosed in housings to further protect them from external light. Each detector (consuming less than 10 watts) is powered by solar panels and communicates via microwaves with the central data acquisition system (CDAS). Inter-detector relative timing uses individual Global Positioning Satellite (GPS) receivers. See Figure 1.9 for a schematic overview of a SD counter [10].

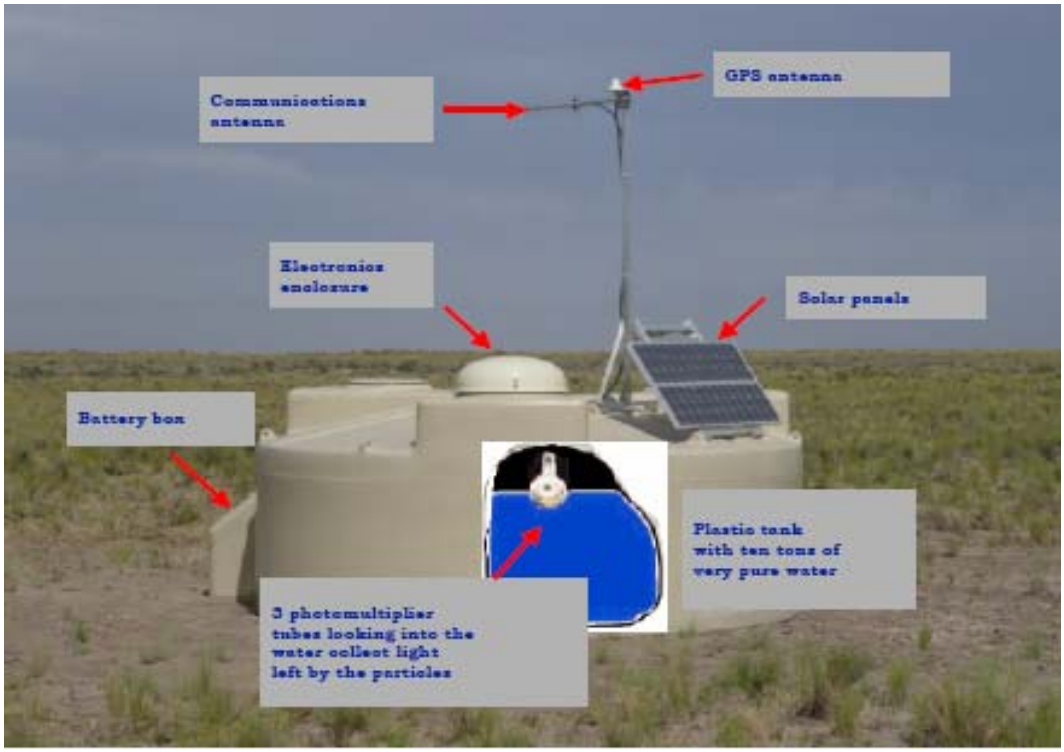

Figure 1.9 Structure of a water Cherenkov counter.

Each tank forms an autonomous unit, recording signals from the ambient cosmic ray flux, independent of the signals registered by any other tank in the SD array.

1.2.3 Electronics and data acquisition

Each tank produces six signals, one from the anode and one from the last dynode of each PMT. The PMT photocathodes are grounded to avoid micro-sparking across their glass envelope. The signals are amplified in fast preamplifiers, the dynode signal being ultimately some 30 times large than the anode signal (the idea being to cope with the problem of possible saturation for large signals). They are read out using a fast circuit containing six 10 bit Fast Analog to Digital Converters (FADCs) running at 40 MHz (25 ns bin). The digitized signals are sent to a daughter programmable logic device board which is used to implement the various triggering decisions [10].

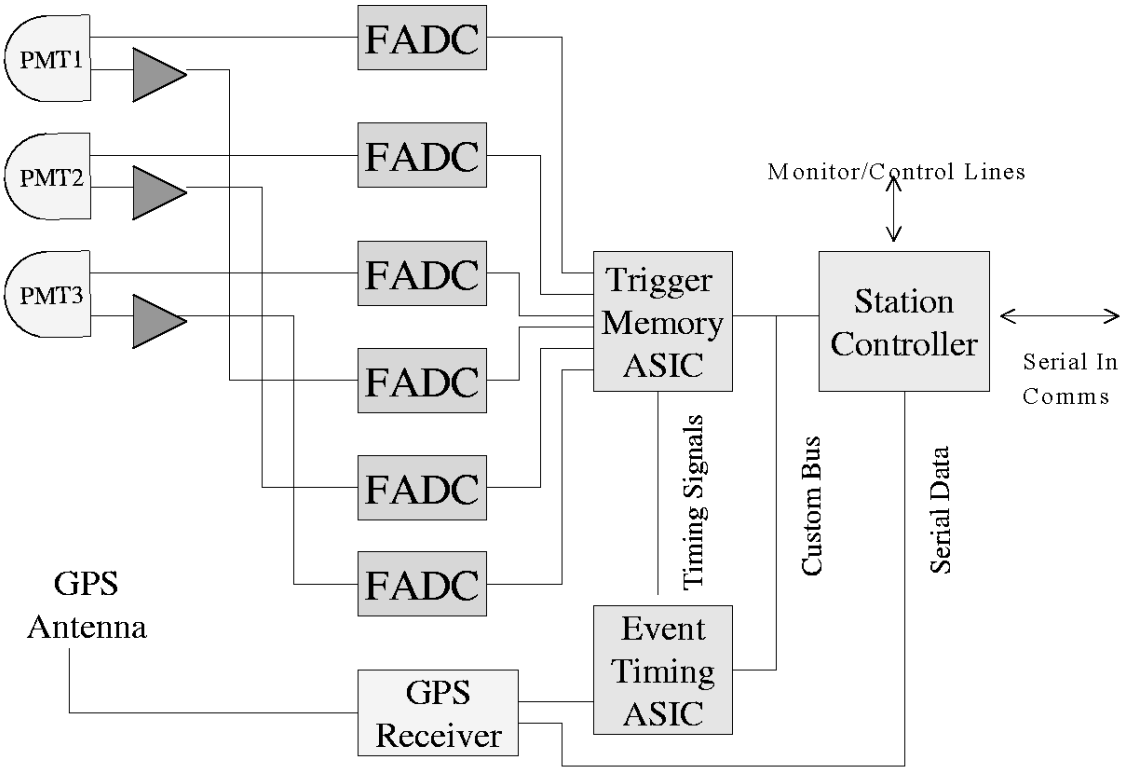

Figure 1.10: Block diagram of the station electronics

Different modes can be used for the first level (T1) trigger. The first uses a 'single threshold'. In this mode, one looks for a coincidence of some PMTs

above a threshold. The second mode uses the ‘time over threshold’ in which a specified number of 25 ns bins are each above a threshold value within a pre-determined time window. A further trigger mode, based on the sum of the signals, can be programmed.

A station controller is used to select events and forward them to CDAS. The station electronics is packed in a metallic enclosure protected by a plastic box placed on top of one of the PMT covers (Figure 1.10).

1.2.4 Calibration

The primary physics calibration required from the SD is the average charge measured for a vertical central muon. It is called a VEM (vertical equivalent muon) [9]. The distribution of the light from atmospheric muons produces a peak in the charge distribution at Q_{VEM}^{peak} corresponding approximately to 1.09 VEM for the sum of the 3 PMTs and to 1.03±0.02 VEM for each individual PMT, as measured using a trigger scintillation telescope in a reference tank [12]. Atmospheric muons also produce a peak in the pulse height distribution (at 1 VEM-peak). The latter is used as the common reference unit for threshold levels. Charge and pulse height histograms produced by a surface detector are shown in Figure 1.11.

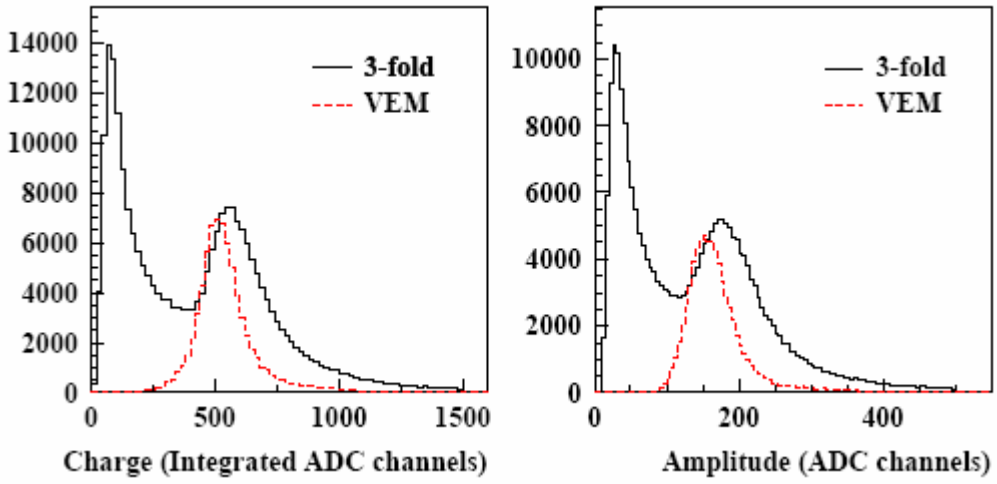

Figure 1.11 Charge and pulse height histograms from a SD station, triggered by a 3-fold coincidence between all 3 PMTs at a trigger level of 5 channels above baseline (full line), or by a small telescope (dotted line). The abscisssa is for the sum of the three PMT signalx

The SD electronics is able to continually perform a local calibration to determine the proper trigger level in electronic units. In addition, it can initially set up the gain of the 3 PMT to be roughly equivalent in order to allow for proper dynamic range and signal sizes for the electronics.

The three main steps of the calibration are:

- The gain of each of the 3 PMTs is preadjusted by matching their rates above a given threshold to a given reference rate measured in a reference tank calibrated from its charge histogram as described above.
- Once the gains of the 3 PMTs are set up, their drifts are monitored and eventually compensated to ensure that the surface array triggers uniformly. This is done by adjusting the trigger levels rather than the PMT high voltage. Histograms are collected over 60 second intervals – approximately 150,000 entries per histogram – and sent to CDAS.

1.3 Data analysis

1.3.1 Direction measurement

Particles scatter from the region of the shower axis throughout its development. The shower core effectively acts as a moving point source of particles which make their way to detectors far from the core. The plane tangent to the shower front at the axis is the shower plane. The shower front itself is slightly curved. Particles far from the core will therefore arrive behind the shower plane.

When three ground stations detect a shower, its direction can be calculated from the arrival times of the signals under the assumption of a plane shower front moving at speed of light. When more than three stations trigger, a least squares method is used to find the shower front which fits best and its curvature can be evaluated.

A crude initial estimate of the position where the shower core impacts ground is the “center of gravity” of the tank signals. Using the shower direction determined previously and this estimate of the core impact, the lateral distance (from the shower axis) of each detector can be calculated. Reconstruction then proceeds by fitting the measured detector densities to an empirical lateral distribution function (LDF), the most probable core impact position and shower size being sought. The procedure can be iterated. It is of course essential that the lateral distribution function be well known. It uses results from previous experiments and detailed Monte Carlo simulations [4].

The precision improves with the size of the shower as a greater number of particles give a better measure of the passing shower front and because more ground stations can be used in the fit. The uncertainty on the core impact position decreases from 80 m to 50 m over the range of relevance.

Muons tend to arrive earlier than electrons and photons, because they suffer much less scattering and so have more direct paths to ground. Heavier ion showers, which are both muon-rich and have developed higher in the atmosphere relative to proton showers of a same energy, have a signal which arrives over a shorter time. The corresponding rise time is therefore an indicator of the nature of the primary.

1.3.2 The measurement of the energy

While the longitudinal shower profile measured by fluorescence detectors provides a nearly model independent measure of the shower energy, ground arrays evaluate the shower energy from the lateral distribution profile, that is the particle density in a plane normal to the shower axis at radius r from it, $S(r)$. Traditionally, they summarize this information in a single number by interpolating and/or extrapolating their measurements to a single radius which is known from shower simulations to correlate well with total energy for all primary particle types. Because of the large spacing between particle counters in the PAO ground array, densities are given at 1 km from the core rather than at 600 m as in earlier arrays. In the determination of the shower energy, there are numerous advantages in the Auger detectors hybrid configuration, a shower measured in hybrid mode having an internal consistency check on the energy. In Auger, the lateral distribution function is approximated by a form $S(r(km)) = S(1000)\ r^{-\nu}$ with $\nu = 4.8 - 1.26\sec\theta$ and the shower energy is inferred from the relation $E(EeV) = 0.12\left(\sqrt{1+11.8(\sec\theta-1)^2}\ S(1000)\right)^{1.05}$ [9].

Chapter 2

The main VATLY Cherenkov Counter

2.1 A summary of the first results

In order to acquire some familiarity with the behavior and performance of the Auger surface detector, a replica of one of its Cherenkov tanks has been constructed and installed on the roof of the VATLY laboratory (located at INST, Hanoi). Its response to muons has been studied using a trigger provided by a scintillator hodoscope [13] located below it (Fig. 2.1).

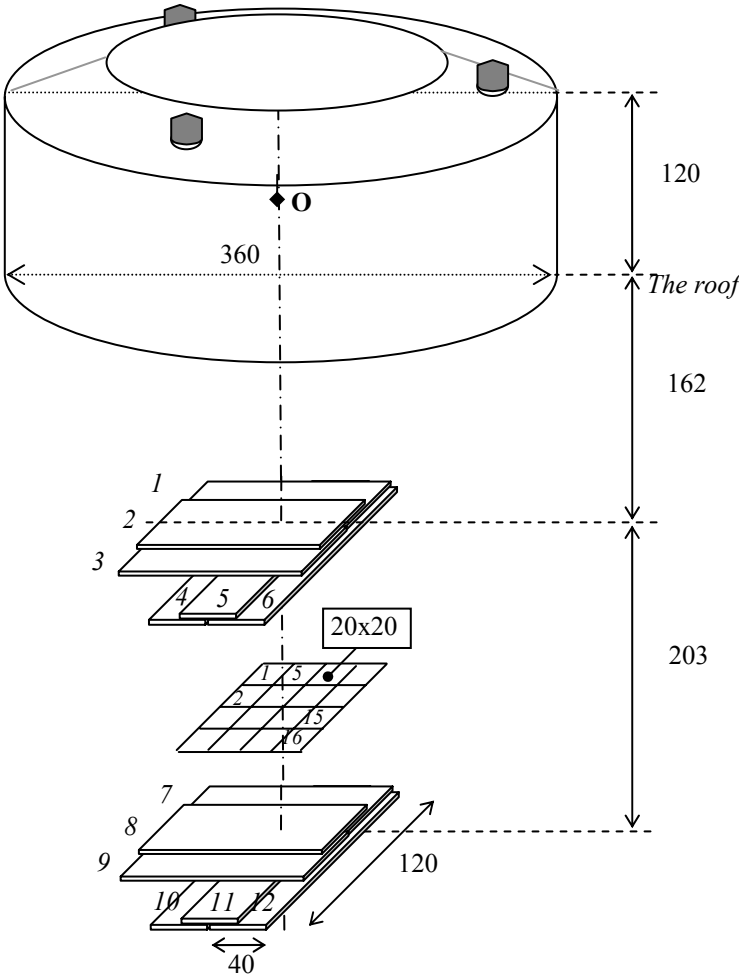

Figure 2.1 Schematic drawing of the setup (distances in centimeters).

2.1.1 Design of the Cherenkov counter

We have constructed a replica of one of the 1600 Auger surface detectors on the roof of our laboratory in order to get familiar with its behavior and performance [14]. The detector is a water Cherenkov counter using three 8” photomultiplier tubes collecting, from the top of the tank, the Cherenkov light diffused on its white painted stainless steel walls. A study of its response to muons was performed using a movable scintillator hodoscope located below it in the laboratory. It was fragmented in such a way as to allow for 256 effective muon beams, impacting the tank in different positions and under different incidence angles (Fig. 2.1).

2.1.2 Electronics

Each PMT signal was resistively split in two equal parts, one being analyzed in an analog to digital converter (ADC-LRS 2249A, 0.25pC per channel) and the other used to feed a discriminator having an input threshold of 10 mV and giving output NIM signals of 40ns width, one of which is sent to a time to digital converter (TDC-LRS 2228, 0.5ns per channel) (Fig. 2.2). The discriminator signals of the hodoscope PMT’s are also used to produce a trigger using the even layers exclusively (each layer signal being obtained by ORing the signals of the two plates in the layer). A trigger on through-going muons requires a fourfold coincidence between the four layers while a trigger on stopping muons requires only a threefold coincidence between the three uppermost layers. The final trigger pulse is broadened to 100 ns in order to provide a gate for the analog to digital converters. It is also used to start the time to digital converters.

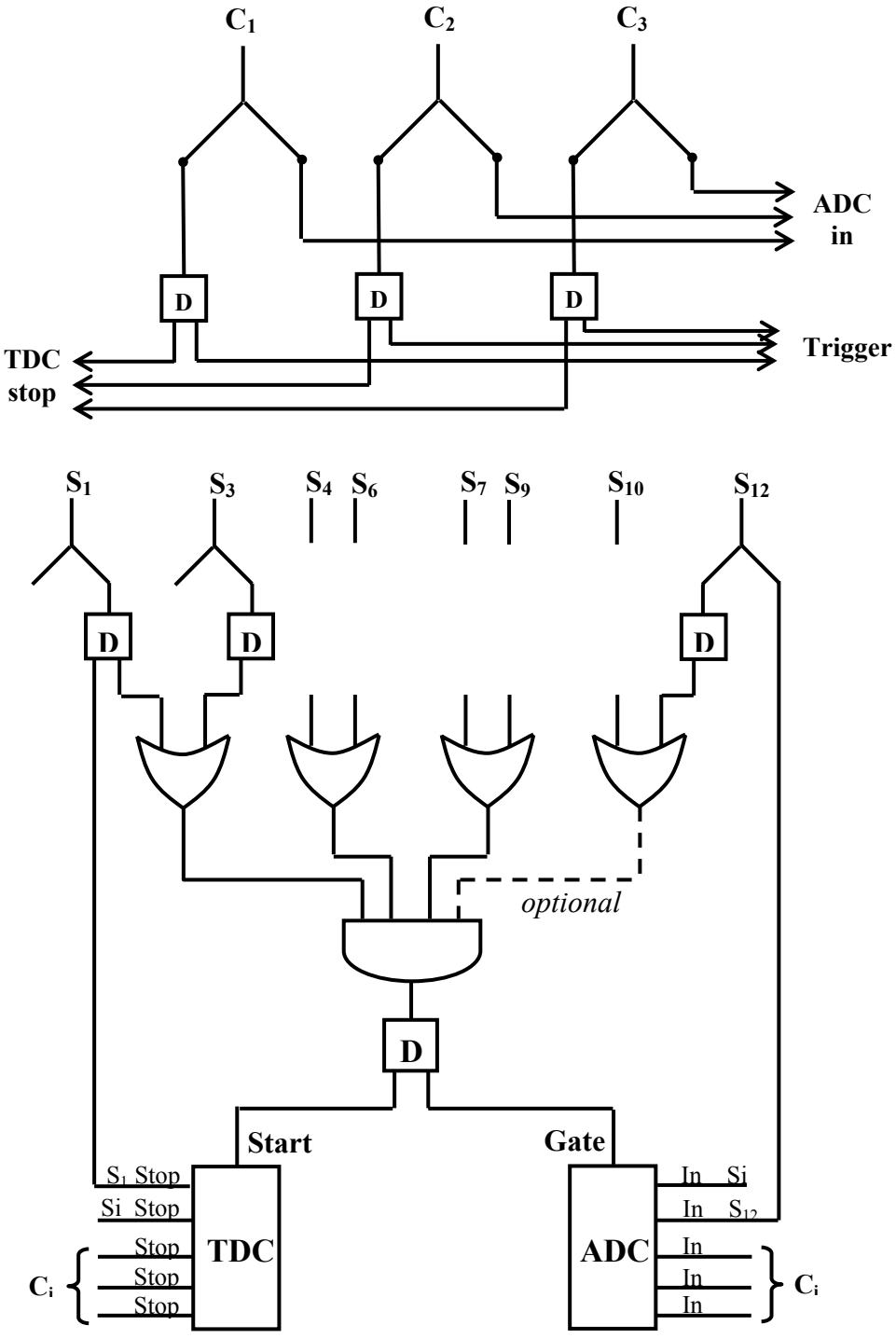

Figure 2.2: Schematic diagram of the electronics

2.1.3 Experimental method

The response of the VATLY Cherenkov counter has been studied using atmospheric muons as a probe. The hodoscope system described in the previous part was used to select such muons. For a muon to give a trigger in the scintillator hodoscope (~ 25 g/cm^2) it must have at least 160 MeV/c when entering it. This corresponds to a β of 0.83 and this muon is therefore essentially relativistic. Taking into account the water Cherenkov counter (~120g/cm^2) and the roof of the laboratory (~ 45g/cm^2) the muon must therefore have at least 500MeV/c when entering the Cherenkov tank. This is much lower than the average muon momentum (4800MeV/c), implying that most crossing muons are highly relativistic. The hodoscope allows for the definition of 16×16 = 256 different "beams" having a typical cross-section of 1600 cm^2 in the medium plane of the Cherenkov counter (see Figure 2.3). Moreover, the lower hodoscope counters can be moved around in order to vary the mean incidence angle. In practice three different geometries have been used: central (vertical incidence), west and north (average zenith angles of ~ 30^o). The hodoscope coincidence was used as a trigger and to open the ADC 100ns gate and start the TDC's.

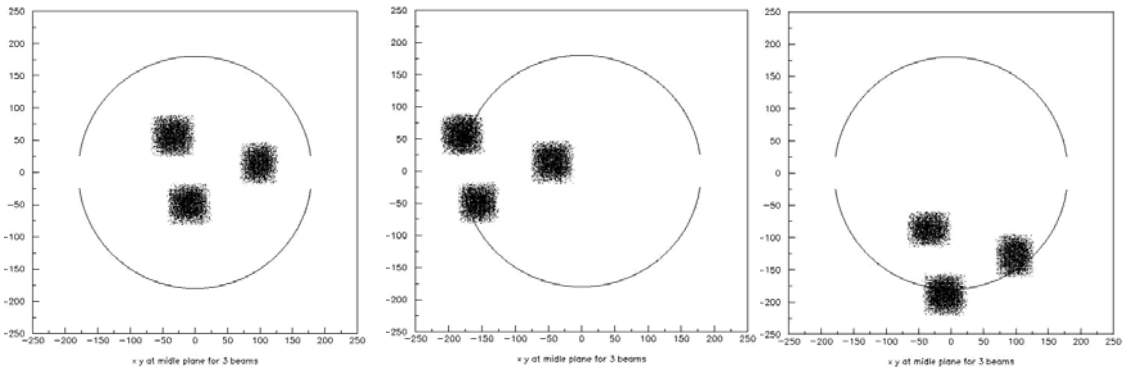

Figure 2.3 Impacts of three of the 256 possible "beams" on the middle plane of the counter for the central, west and respectively north geometries (from left to right).

2.1.4 Response to muons and dependence on track length

Vertical muons have been studied in the central geometry where the track length in water remains very close to 120 cm. We define "good muons" as having an average hodoscope pulse height between 0.6 and 1.5 minimum ionizing particle equivalent (mip) [13] and an average hodoscope time of flight (between the upper and lower scintillator stacks) between 0 and 12 ns. Three quarters of the events were associated with high pulses in each of the three Cherenkov PMT's. Low pulses were found to be nearly uncorrelated and to be usually associated with late times. The main results are summarized in Table 2.1 and in Figures 2.4 and 2.5. The width of the measured Cherenkov spectra is exclusively due to the relatively small amount of light collected in each PMT. Even in the case of three good PMT's (55% of the events) the ratio rms/mean is 42% compared to 15% in the PAO, suggesting that we collect 8 times less light (of which a factor 1.3 is accounted for by the different photocathode diameters).

Table 2.1

Number of "good PMT's"	Number of events	*Rms*/mean (%)	$\sim n^{-1/2}$
3	788 226 (55%)	42	40
2	539 062 (37%)	48	49
1	104 815 (7%)	67	69
0	8 728 (1%)	-	-

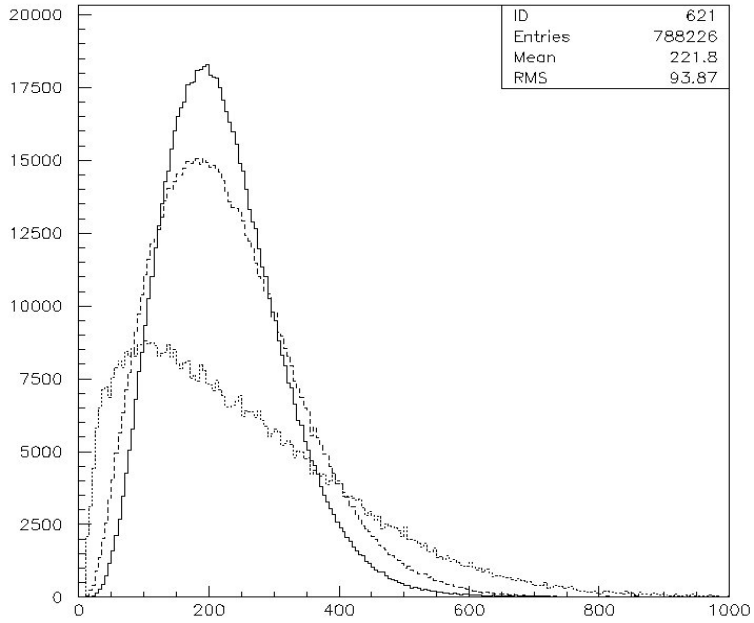

Figure 2.4: Pulse height distributions of events having 3 (full line), 2 (dashed line) and respectively 1 (dotted line) "good PMT's". The plotted pulse height is the average of the "good PMT's" pulse heights. The 2 (respectively 1) "good PMT's" data have been multiplied by 1.5 (respectively 6) for convenience.

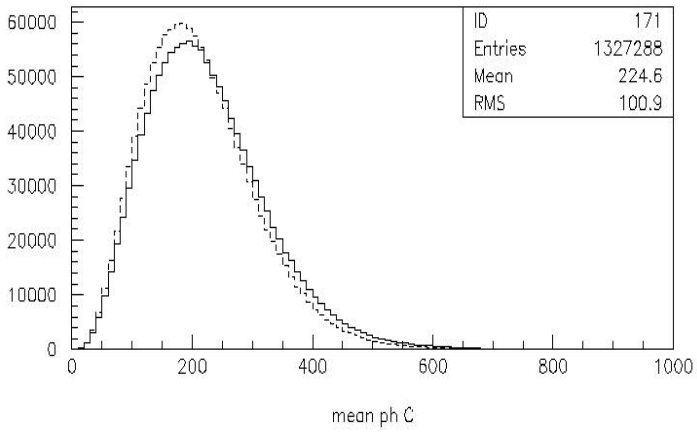

Figure 2.5: Pulse height distribution for good muon events having at least two good PMT's averaged over good PMT's. Full (dashed) line is for uncorrected (d-corrected) data.

In order to study the track length (l)-dependence, we use instead the west and north geometry data samples where l covers its full spectrum. All "good

muons" events having $l > 20$ cm have been retained. We find that for low l values, there is a very high probability to have low PMT signals (Figure 2.6). A linear dependence of the signal on l gives a good fit to the data, as illustrated in Figure 2.7. However, in the central geometry, correcting for the small spread of the track lengths does not bring a significant improvement to the data of Figure 2.5.

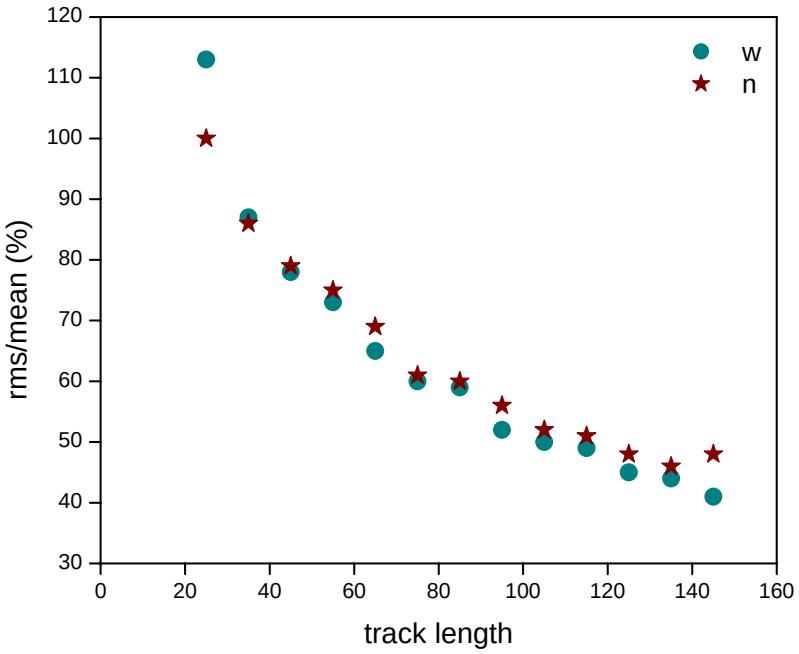

Figure 2.6: Relative widths of the pulse height distributions as a function of track length. West (circles) and north (stars) data are shown together.

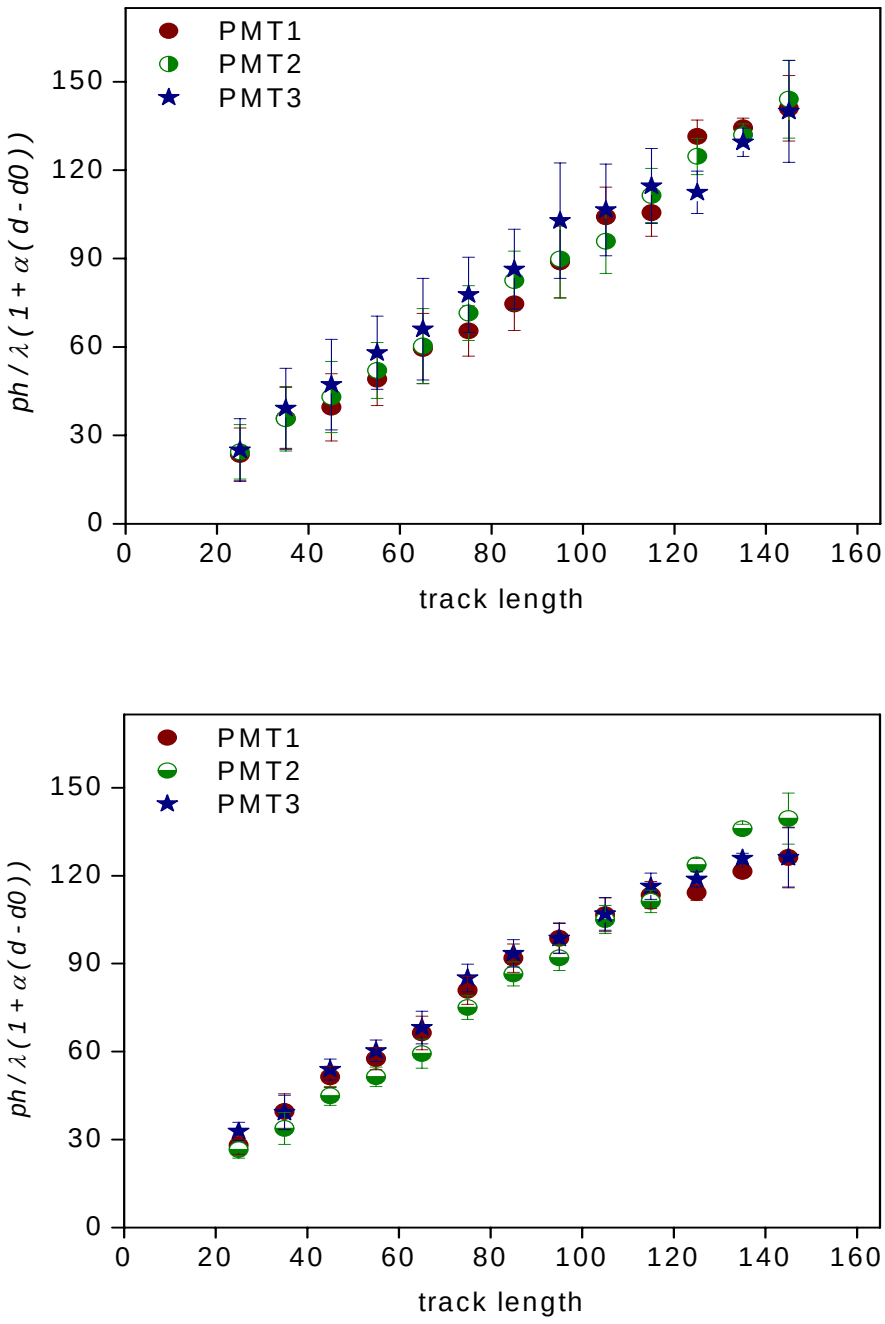

Figure 2.7: Dependence on track length of the mean value of the pulse height for the west and north data respectively.

2.1.5 Conclusion of the early studies

The study of the Cherenkov response to atmospheric muons has shown a number of features that may be briefly summarized as follows:

– The pulse height spectra measured in each phototube depend in a clear and well understood way on track length and on the proximity of the track.

– Pulse height spectra are too wide and too low compared to what they should be. From the value of *rms*/mean=48% for vertical muons and 3 good PMTs, compared to the Auger [12] equivalent number of 15%, we deduce that we have $(48/15)^2$=10 times less photoelectrons in VATLY than in Auger. Assuming a factor 2 in photocathode efficiency and accounting for the factor 1.3 in photocathode area, we deduce a deterioration factor of 10/2.6 = 4 resulting from the lower water transparency and the worse wall diffusivity.

– The poor resolution precludes the use of an efficient correction algorithm allowing for improving it. Indeed, taking the average of the three PMT pulse heights (which boils down to increasing the collected light by an average factor of three) is the best one can do.

A parallel study (see below) has shown that the PMT's suffer an important after-pulsing, most likely due to the presence of gas in the glass envelopes. This should not, however, cause an important deterioration of the resolution. The purity of the water and the quality of the diffusing surface of the tank walls are much more likely candidates to explain the low value of the light collection.

2.2 After pulsing

While attempting a measurement of the muon lifetime by detecting successively the Cherenkov signals of a stopping muon and of its decay electron, we have noted the presence of after pulses which disturb this measurement. As we suspected fluorescence of the white paint coating the walls of the counter to be the source of this effect, we have set up a small experiment in order to check this hypothesis. As we will see in what follows after pulsing was revealed in many different experimental arrangements and the fluorescence hypothesis turned out to be wrong (at least at a significant level) [15]. In all cases which have been investigated we found that after pulsing occurs at a few percent level and seems to take place in the PMT and/or PMT base rather than in the detecting medium (scintillator or Cherenkov tank). The remainder of this section is dedicated to a description of the measurements performed and of their results.

2.2.1 Experimental setup

We first used two similar plastic scintillator plates, 52×54×3 mm^3. One of them was painted with a thin layer of the white paint used to coat the inner walls of the Cherenkov counter. The other was simply wrapped in an aluminum foil as usual. Figure 2.8 shows the experimental arrangement.

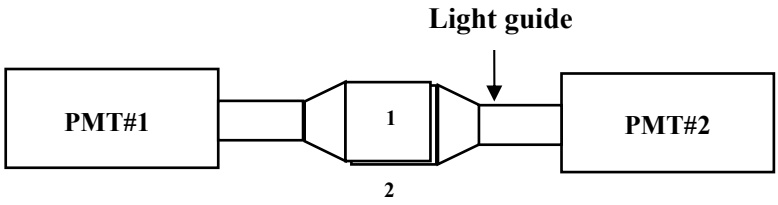

Fig 2.8: Configuration
1: Painted
2: Not painted

The two scintillator plates can be moved around easily, thereby allowing for different directions of incidence of the particles traversing both plates. In the standard position they overlap exactly and are separated by a vertical distance of about 2 mm.

Each scintillator plate is seen by a single 2" PMT. The working high voltage is set at 2150 V on plateau. The electronics diagram associated with these counters is shown below (Figure 2.9).

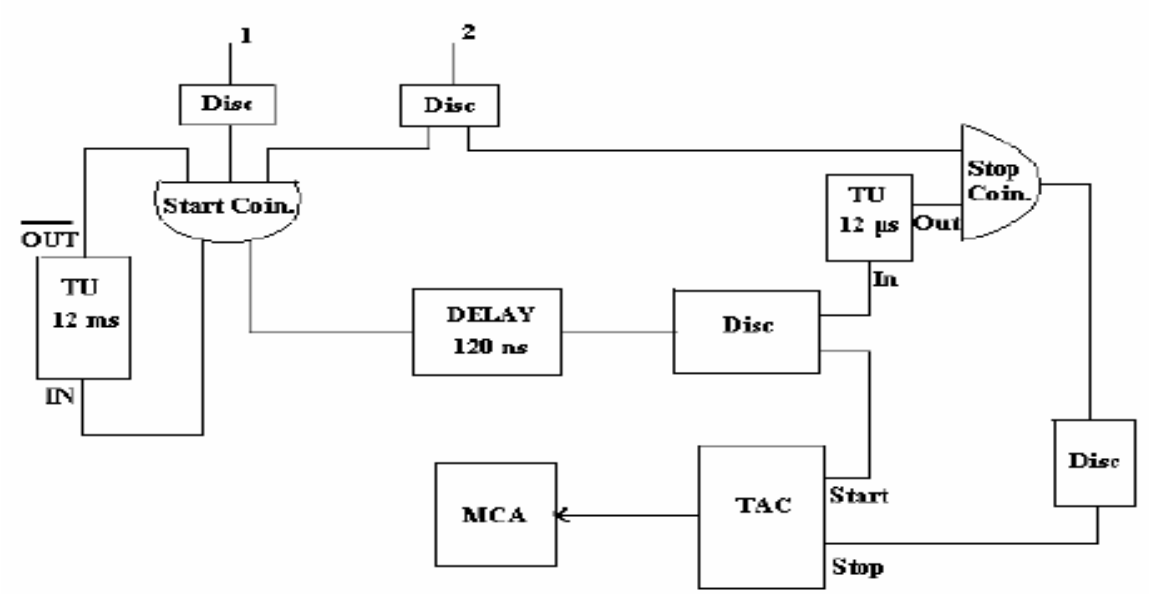

Fig 2.9 Electronics principle diagram in normal data taking

The PMT signals are sent to discriminators having their threshold set low (50 mV) via cables adjusted to have a good coincidence timing (24 and 16 ns respectively). A 1-2 coincidence is used to start a time-to-amplitude converter (TAC), and counter 2 to stop it. The TAC output signal is then sent to a multi channel analyzer (MCA). A dead time of 12 ms is introduced at the level of the start signal in order to guarantee a smooth functioning of the TAC. Similarly, a window of 12 µs is used on the stop signal. Both of these are generated using standard timing units. Whenever necessary, delays and

pulse regenerators (discriminators with a high threshold set at 170 mV) are introduced as shown in the figure. When changing the nature of the start and/or stop signals the protecting features (dead-time and stop window) are always maintained.

The essential component of the measurement is the TAC, an electronic unit that measures the time elapsed between the arrival of two pulses at each of its inputs, the "start" and the "stop". The output is a third pulse that has standard width but the height of which is proportional to the time difference between the start and stop pulses. It is subsequently analyzed in the MCA that records its pulse height distribution, namely the distribution of the time differences between the start and stop signals.

Calibration of the time scale is made using a same pulse at the start and stop inputs, the later being delayed by a fixed known amount. In addition, a lower level discriminator (LLD) used to kill a possible TAC noise was set at about 50 channels. The upper level discriminator (ULD) was set at maximum. The result of the calibration is that the MCA is reasonably linear with about 5ns per channel.

2.2.2 Definition of variables

In normal data taking, the TAC start is the 1-2 coincidence while different TAC stops have been used.

In the absence of correlation between the start and stop signals, the number of stop signals ignoring the 12μs window has a time distribution of the form

$$\frac{dN_{stop}}{dt} = N_{start} R_{stop} \exp(-R_{stop} t).$$

The presence of the window does not change the shape of this distribution but simply cuts it off. The number of events recorded in the MCA is therefore the integral of this distribution between 0 and T_{window} namely $N_{stop} = N_{start}\left\{1-\exp\left(-R_{stop}T_{window}\right)\right\}$ which reduces for $R_{stop}T_{window} << 1$ to $N_{stop} = N_{start}R_{stop}T_{window}$. In fact the integral should start at 250 ns corresponding to the 50 channels LLD setting.

Here the number of start events, N_{start}, is the product of the time T during which the MCA is accumulating data by the effective start rate R_{start}. R_{start} is in fact the raw start rate R_0 divided by $1+T_{dt}R_0$, where T_{dt} is the dead time. R_{stop} is the raw stop rate, ignoring T_{window}. These relations allow for an evaluation of the fraction of correlated stops:

$$\rho = \frac{\left(N_{MCA} - N_{start}\left\{1-\exp\left(-R_{stop}T_{window}\right)\right\}\right)}{N_{MCA}}$$

2.2.3 Scintillator data

Data were taken using a Cesium 137 source in two different configurations: first with the painted scintillator on counter 1, then on counter 2. Figure 2.10 shows that PMT 1 has a “bump” independently from which scintillator is attached to it. Moreover, ρ increases from 17% to 20% (PMT 1) and from 6% to 13% (PMT2) when going from the painted to the unpainted scintillator. This shows unambiguously the absence of any significant fluorescence effect due to the white paint. Moreover a simple explanation can be devised if we assume that the ensemble PMT+base is solely responsible for the observed after pulsing. Then, remarking that the painted scintillator is

expected to produce less light than the unpainted one and, assuming that after pulsing increases with the amplitude of the initial pulse we can reproduce, at least qualitatively, the observed data. Here a given PMT is in fact a set phototube + base that were never separated.

Figure 2.11 compares spectra (counter 2 and painted scintillator) taken with cosmic muons and with the source. We find that ρ is about twice as small for muons, again consistent with the fact that muons are minimum ionizing and therefore expected to give a lower signal.

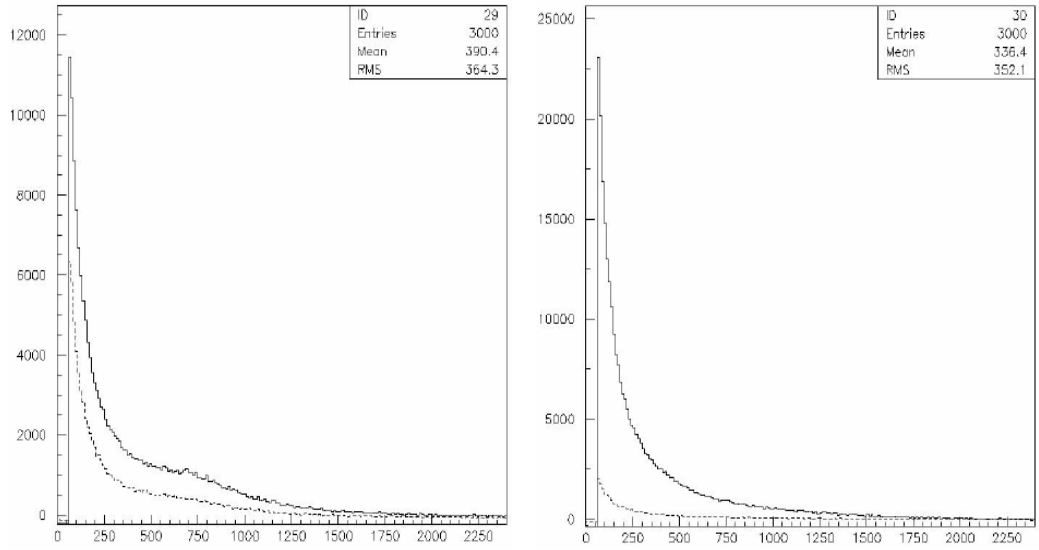

Figure 2.10 MCA spectra obtained with PMT 1 as stop (left histograms) and PMT 2 as stop (right histograms). The painted scintillator data are the upper curve in both cases.

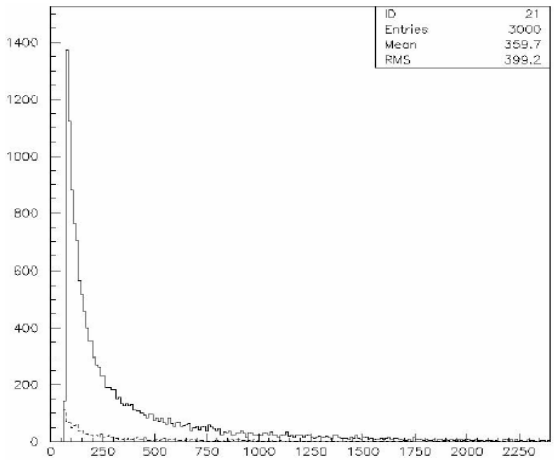

Figure2.11Muon source comparison

In conclusion the data suggest that the observed after pulsing is a general feature of our PMT's and has nothing to do with the type of detector attached to them. Moreover we find an indication that the after pulsing probability increases with the pulse height of the initial pulse.

As a check, we measured how much after pulsing there is in our standard hodoscope. Data were taken with counters 1, 2 and 4 in coincidence (a 20×40 cm^2 rectangle) as start and one of the counters (1 or 4) as stop. We find ρ values of 1.7% and 5.4% respectively.

2.2.4 Data taken with the Cherenkov PMTs

On the basis of the above results, we went on to study the Auger Cherenkov counter in order to understand what is causing its PMT's to after-pulse.

A first series of measurements were made by starting the TDC with a four layer hodoscope coincidence as described in section 2.1 and stopping it

with one of the Cherenkov PMT's (counters 22 and 23 were measured). In this case we look at cosmic muons that traverse the Cherenkov counter: no decay can have taken place. The measured spectra are shown on Figure 2.13 and 2.14.

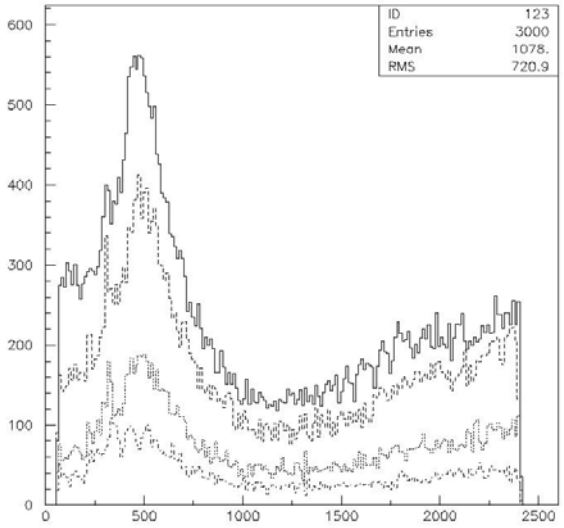

Figure2.13 Counter 22 at different high voltages (HV=2.0, 1.9, 1.8 and 1.7 kV from top to bottom.

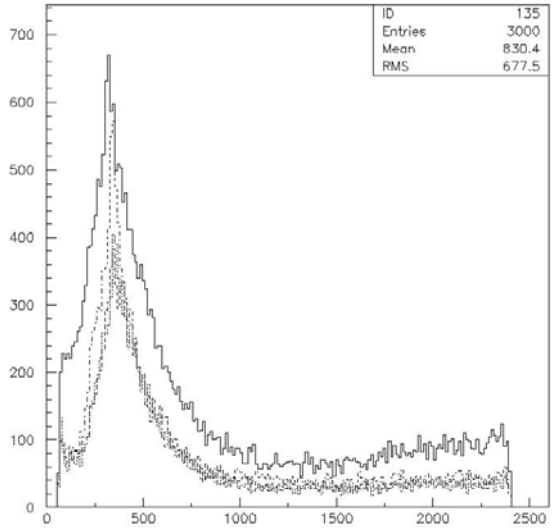

Figure2.14 Counter 23 at different high voltages (HV=2.0, 1.9, 1.8 and 1.7 kV from top to bottom.

From these measurements the following observations can be made:

There is after-pulsing in all cases. It consists of a first broad bump centered around 2μs followed by a tail. The detailed shape of the bump depends on the PMT+base system (in particular there is a

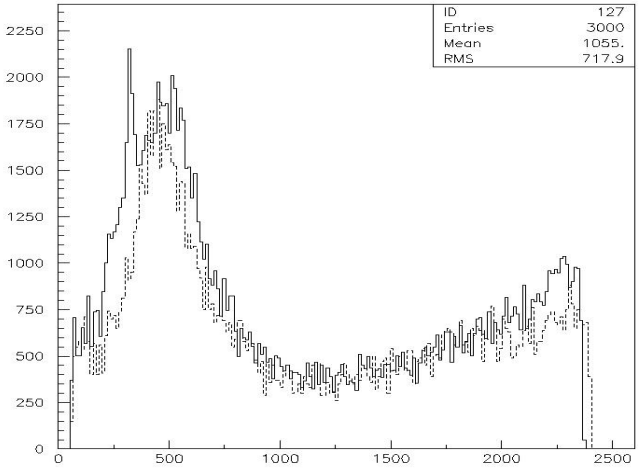

Figure2.15 Spectrum of PMT 22 using base 23 (dotted line) or base 22 (full line) at 1.8 kV

narrow peak at 1.5μs in 22 but not in 23 and the main peak positions are different) but not on the value of the high voltage. The tail increases with high voltage and has not decayed at the end of the 12μs window. On the contrary it often keeps increasing at variance with earlier measurements: after-pulsing now extends farther out than the 12 μs window. This makes our way to evaluate the amount of correlation inadequate.

Moreover we found that the spectrum of PMT 22 is unchanged when we use the base of counter 23 rather than the base of counter 22 (Figure 2.15) except that a narrow peak that was present around 1.5 μs has now disappeared. Moreover, as these data were taken at 2.1kV (Figure 2.16), the tail is now smaller (and even more so for the hodoscope.22.23 trigger): it is at the same level as it is for 1.8kV in Figures 2.14 and 2.15. The ρ parameter increases from 0.2% to 0.9% when adding the hodoscope 4-fold coincidence to the start coincidence.

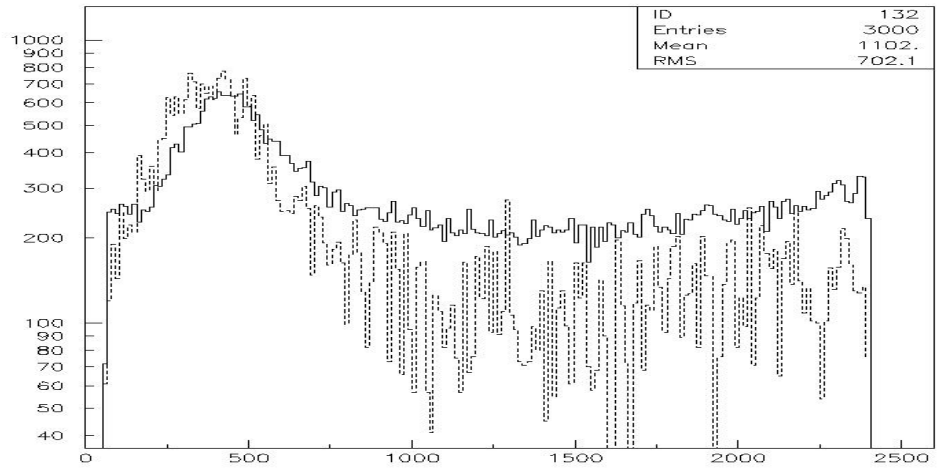

Figure 2.16 Stop with 22.23 and start with 22.23 (full line) or ABCD.22.23 (dotted line) at 2.1 kV.

The study was repeated using a new PMT of the same type as that used in the Cherenkov counter but located in the lab. It was attached to the base of counter 22 and enclosed in a light tight mu-metal cone (as used in the Cherenkov counter). A small scintillator was placed in front of its photocathode that could be excited using the Cesium source. We recorded the autocorrelation spectra of the new PMT for different high voltage values. After pulsing was again observed, similar to the Cherenkov PMT data, but the structure was significantly different, with a lower tail and multi-peaked.

2.2.5 Dependence of the start and stop rates on dead time and window widths

In order to evaluate the duration of the after-pulsing (at this stage we only know that it extends beyond the 12μs window) we measured the start and stop rates by varying the widths of the dead-time (and respectively window) timing-units. The results are shown in Figure 2.17 and were analyzed assuming an exponential shape of the after-pulsing distribution in time, $\frac{dN}{dt} = \left(\frac{1}{\Delta t}\right) P e^{-t/\Delta t}$. We neglected events with more than a single after pulse. Calling R the rate of master pulses, the expressions for the start and stop rates are:

$$R_{start} = \frac{1 + P e^{-W_{DT}/\Delta t}}{\frac{1}{R} + W_{DT} + P\left(\Delta t + W_{DT}\right) e^{-W_{DT}/\Delta t}}$$

$$R_{stop} = \frac{RW_{WD} + P\left(1 - e^{-W_{WD}/\Delta t}\right) + PRW_{WD}\left(\left(\frac{W_{DT} - T_{cutoff}}{W_{DT}}\right) e^{-T_{cutoff}/\Delta t} - \frac{e^{-T_{cutoff}/\Delta t} - e^{-W_{WD}/\Delta t}}{W_{WD}/\Delta t}\right)}{\frac{1}{R} + Max\left(W_{WD}, W_{DT}\right)}$$

where W_{DT} is the width of the dead-time timing unit, W_{WD} is the width of the window timing unit and T_{cutoff} (=3μs) is the smallest separation time

acceptable by the scaler (two pulses separated by less than T_{cutoff} are counted as a single one).

The best fit is obtained for $R = 212Hz$, $P = 10.8\%$ and $\Delta t = 8.35\mu s$. The value of W_{DT} used during the R_{stop} measurements had not been exactly measured (it was approximately 12ms). Therefore we also fit it with the result $W_{DT} = 13.1ms$.

We retain from this study that after pulsing occurs at a rate of about 10% and lasts over some 8 µs.

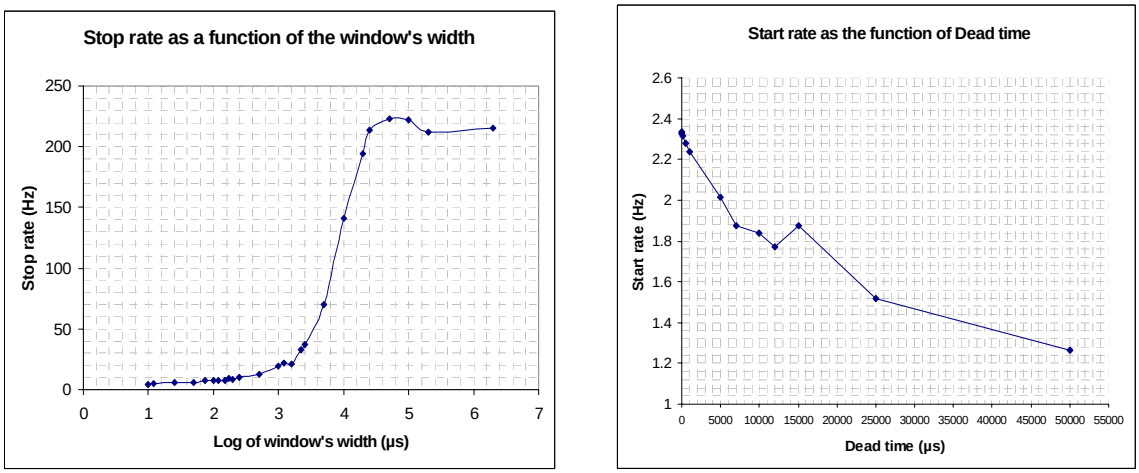

Figure 2.17: The dependence of the start and stop rates on w_{DT} and w_{WD} respectively.

2.2.6. PMT divider chains and possible microsparking

As the long duration of the after-pulsing might have suggested that it was due to microsparking either in the base or in the PMT, we decided to check this hypothesis. If sparking takes place in the PMT, we would expect it to be very different if we ground the anode rather than the cathode. This was done using a new base with the result that no significant difference was observed, making it unlikely that sparking was the cause.

We have inspected the exact design of each of the PMT bases that have been used. It can be separated in three parts: the output stage on the anode, the input stage on the photocathode and the voltage divider in between. Figure 2.18 shows such a design (base 24).

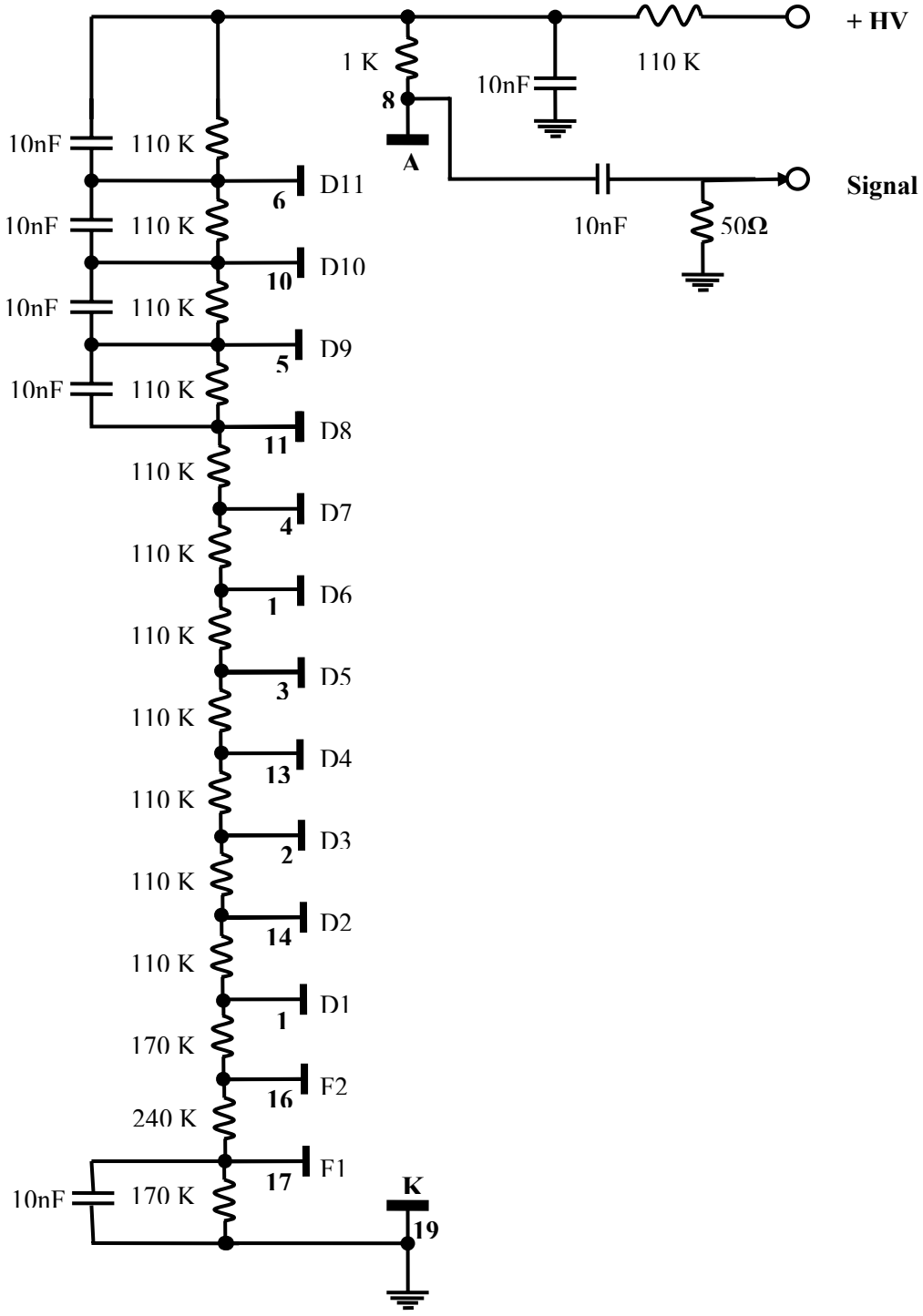

Figure 2.18: The electric diagram of base 24.

The input stage starts with the grounding of the photocathode (important to prevent microsparking). There are two focussing grids that are internally connected to later dynodes and two focussing electrodes that are accessible. In some bases they were left floating while in some others they were connected onto the divider chain.

The output stage includes the signal coaxial cable that is terminated on 50 Ω and connected to the anode through a 10000 pF capacitor (to isolate the front end electronics from high voltage!). The HV is fed through a resistor (100K typically) for safety. The last dynodes are bridged with capacitors in order to integrate the pulse at high current values. Most bases have a linear chain.

When changing from positive to negative HV, all that needs to be done is to connect the HV connector to the photocathode (and disconnect the photocathode from ground!) while at the same time removing the capacitor between the anode and the signal cable.

The inspection of the bases has not revealed anything that might have caused after pulsing. On the contrary, the fact that each base was slightly different from the others, and the fact that they all are associated with after pulsing, suggests that their exact design is somehow irrelevant.

2.2.7 Conclusion

A possible cause of after pulsing could be the presence of gas in the glass envelopes of the phototubes that are more than thirty years old. This is indeed mentioned in “Techniques for Nuclear and Particle Physics Experiments” by W.R. Leo, page 193, as a known source of after pulsing. The idea is that the residual gas gets ionized and the ions are accelerated toward

the photocathode. They may reach it or be intercepted by a dynode on their way, depending on where they were formed. But whether they land on the photocathode or on a dynode, they will eject electrons that will produce the after pulses. For an ion of mass M (MeV) to travel a distance D (cm) under a field E (V/cm) it takes approximately a time $t(\mu s)=(0.5\ MD\ /\ E)^{1/2}\ /30$. Here we have D/E~100V. For electrons we find 33 ns, for hydrogen, 1.5 μs and for nitrogen, 5.2μs. These numbers are in the right ball park to explain our observations. Moreover the multiple peak structure can very well be explained by the various possible paths between dynodes or between dynodes and photocathode. In particular the fact that slightly different patterns have been observed when changing base or PMT can be easily understood.

A check of this interpretation is to study the dependence of the after pulsing pattern on high voltage V: for a given geometry, in particular a given PMT-base association, we should find ion transit times that are inversely proportional to $V^{1/2}$. Between 2.1 and 1.8 kV we found a 8% effect consistent with expectation.

Having eliminated one after the other all other possible sources which we could think of, and having here an explanation that is consistent with our observations, we retain it as being the most likely explanation. A direct check will be made later on using recently manufactured PMT's.

2.3 Refurbishing the main counter

The VATLY Cherenkov counter has been refurbished in order to improve the light collection efficiency, including the following steps:

– replace the 8" EMI (very old) phototubes by new 9" Photonis phototubes of the type used in the Auger experiment. In this new design,

both the last dynode and the anode signals of each phototube are amplified and analyzed separately.

– coat the inner tank walls with aluminized mylar that should provide a better diffusion coefficient than white paint.

– improve the quality of the water transparency and prevent thin particles to settle down on the floor of the tank, deteriorating significantly its diffusivity.

Before filling the tank the whole system was checked using a scintillator plate on the bottom of the empty tank as a light generating medium. The results of this test was excellent but they will not be presented here.

2.3.1 The new Photonis PMT's

The new Photonis PMT's (Figure 2.17) are PAO phototubes that were rejected as having an insufficiently linear response. Such an effect is caused by a slight imprecision in the last dynode and anode geometry and positioning and is not expected to have other consequences on the behavior of the tube. The fitting of the tubes in the Cherenkov tank have been modified in order to account for the slight difference in tube geometry. The front end electronics used in the PAO, (with amplifiers on both the anode and dynode signals, the latter giving a typical dynode to anode ratio of 32) is now also being used here, together with a high voltage generator controlled by a 0-12 V signal. The control electronics required for this purpose has been manufactured in the laboratory (Figure 2.18) and is operating properly.

Figure 2.17 Photonis PMTs have been installed in the main VATLY Cherenkov Counter

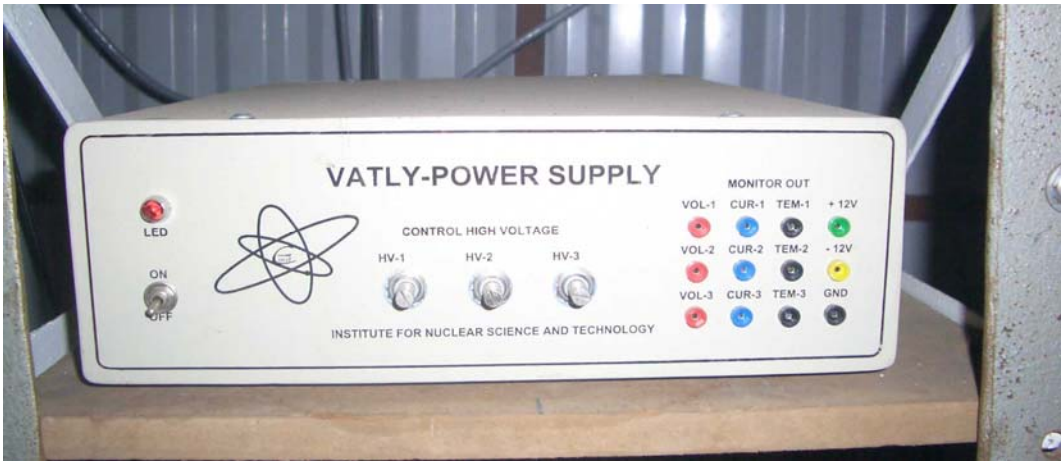

Figure 2.18 High voltage control unit of the PMTs

2.3.2 Water purity

Water purity was a major problem in the early design. Water was taken from the town supply and filtered through standard sand filters down to 10µm grain size. However it was found that it still contained a significant amount of iron oxide in the form of thin dust grains that were settling on the ground plate of the tank and significantly deteriorating its diffusivity. An additional filtering unit has now been added in series (Figure 2.19) that should filter down to 1 µm grain size.

Figure 2.19 Water filter machine

Moreover, faucets have been installed at the top and bottom of the tank to allow for a small water circulation from time to time if necessary in order to evacuate settling dust. Filling the tank is a slow process that was initiated at the end of August 2006 and that will take some two months before being completed.

2.3.3 Wall coating

In order to improve the diffusivity of the tank inner walls, several kinds of coatings have been tried. Using standard commercially available aluminum foils turned out to be impossible as holes were observed to slowly develop in

the foil, possibly produced by the small remaining acidity of the filtered water on impurities in the foils. After several attempts to find a proper coating medium, we have retained adhesive aluminized mylar as the best choice. The side walls, as well as the top and bottom plates of the Cherenkov tank are now coated with such foils. We convinced ourselves that the adhesive glue that backs the foil could not be a source of problem on a reasonably long range.

Chapter 3

The small Cherenkov counters of VATLY

A set of three Cherenkov counters has been assembled around the main VATLY Cherenkov counter in order to detect showers that give signals in all counters simultaneously. The idea is to require a coincidence of the three small counters as a trigger used to study the response of the main Auger counter to showers. In order to have as little trigger bias as possible, we decided to require only a two-tank coincidence in the on-line trigger and to leave the requirement of a three-tank coincidence for the off-line analysis. Indeed the two-tank coincidence rate is of the order of 1Hz and the three-tank coincidence rate is of the order of 0.01Hz, making this trigger strategy very sensible.

The use of three tanks allows in principle to measure the direction of arrival of the shower, implying that the time of arrival of each of the tank signals is accurately measured. Moreover a pulse height measurement of each of the tank signals is desirable in order to study correlations with the size of the signal measured in the main tank. It was decided to equip each tank with a pair of phototubes, a minimum requirement to suppress thermal noise. Moreover, as the online trigger requires only a two-tank coincidence, it is not necessary to allow for a large time difference between the two coincident signals: showers located near the mediator plane of the segment joining the two trigger tanks give equal timings in these tanks while the timing in the third tank may vary over a large range, corresponding to a large range of zenith angles.

The general considerations above dictated the design of the set of small tanks which we are now describing in detail.

3.1 Tank design

The tanks used are 3000 liters standard water tanks equipped with two upper holes used to house the photomultiplier tubes. They are horizontal cylinders with a length of 170 cm and a diameter of 145 cm. They are made of stainless steel and the inner surface quality was considered sufficiently good to use it as such, namely without any additional coating. They were filled with the filtered water that was contained in the main tank where it had time to settle down for nearly two years. The exact location of the tanks is shown in Figure 3.1.

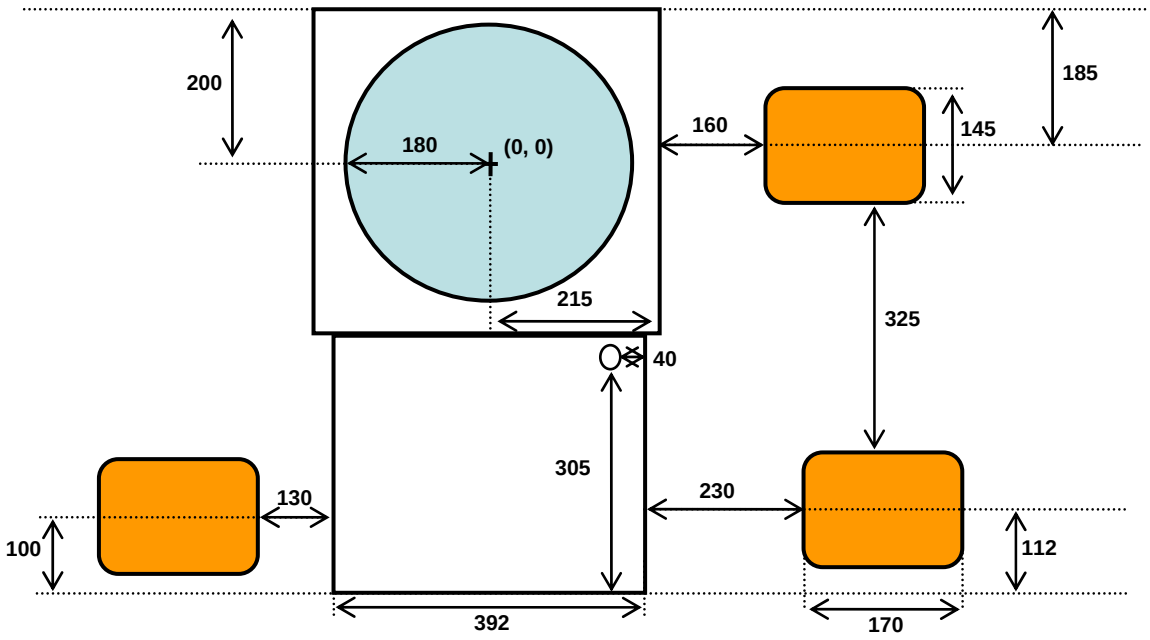

Figure 3.1 : Location of the small Cherenkov tanks

The phototubes are EMI D340A eleven dynodes phototubes having a spherical photocathode of 8" diameter. As explained earlier, the vacuum of these tubes, that are over thirty years old, has somewhat deteriorated, resulting in a significant after pulsing that is however of no harm in the present use. At the same time, the photocathode efficiency can be expected to have deteriorated from the original value of 20% or so to something like 10%. In order to cope with the relatively low number of collected photoelectrons that we can expect, it was decided to amplify each of the phototube signals by a factor 10. A typical track length of 1 m corresponds to some 20000 Cherenkov photons in the case of a vertical relativistic muon. The ratio between the photocathode area and the inner walls area is ρ=0.6%. For a single diffusion, assuming perfect randomization and no loss, we can therefore expect $20000\times\rho\times10\%=12$ photoelectrons. The quality of the water transparency and of the wall diffuseness cannot be expected to allow for more than one effective diffusion. The duration of the light pulse should be expected to be of the order of 10 ns corresponding to a 2m light path in water where the light velocity is 20cm/ns.

In order to avoid microsparking across the glass of the phototube envelope, it was decided to keep the photocathode grounded, implying that the anode must be at some +2kV: the signal must be read out on 50 Ω across a capacitor. In the present design this capacitor has a value of 10^4 pF.

The phototubes are kept in position in such a way that the photocathode is immersed in water. The detailed design of the holding system is shown in Figure 3.2. The signal (50 Ω coaxial) and high voltage cables associated with each PMT are enclosed into light tight PVC tubes that end in the central cabin that communicates with the laboratory through a hole in the roof. While the signal cables go directly to the laboratory, the high voltage cables go to a

distribution panel located in the central cabin. This panel is fed with three independent high voltage cables that split into two: this way we can use a single high voltage supply for two phototubes having similar gains. The high voltage dividers used for this purpose are shown on Figure 3.3.

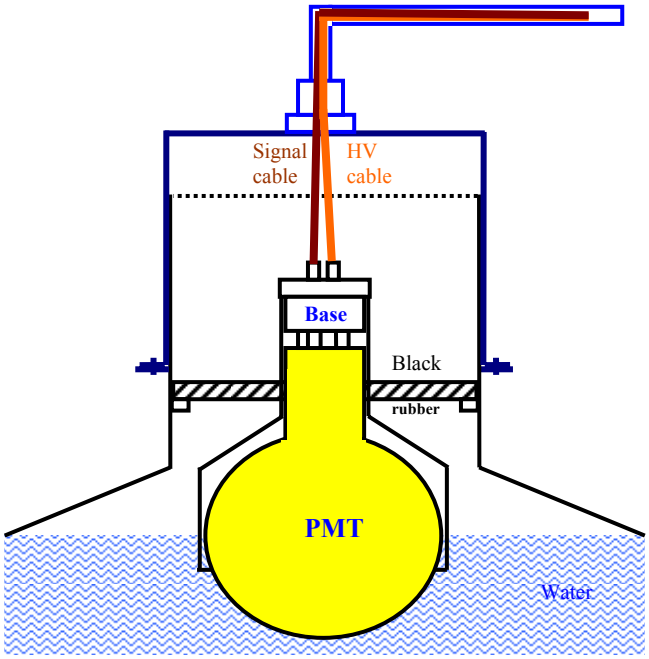

Figure 3.2: Holding system of PMT in the small Cherenkov tanks.

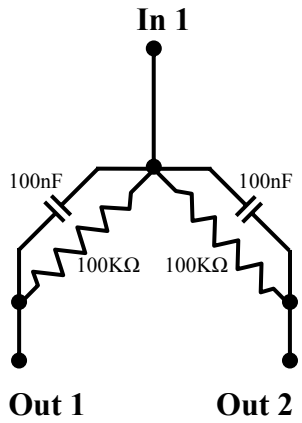

Figure 3.3: Schematic diagram of a high voltage splitter.

3.2 Electronics

Each signal is amplified through a gain 10 fast preamplifier, the output of which is resistively split into two equal pulses. One of these is sent after some delay to an analog to digital converters (ADC) for measuring its charge. The other is sent to a fast discriminator that produces a NIM pulse used for building up the trigger and, after some delay, stopping the time to digital converters (TDC) that are started by the trigger pulse. Both the preamplifiers and the resistive splitters were assembled by us. The schematic drawing of the preamplifier, that uses a AD8012 integrated circuit, is shown in Figure 3.4.

The splitters are simply made of a star of 16 Ω resistors such that each of the three ends sees a 50 Ω impedance.

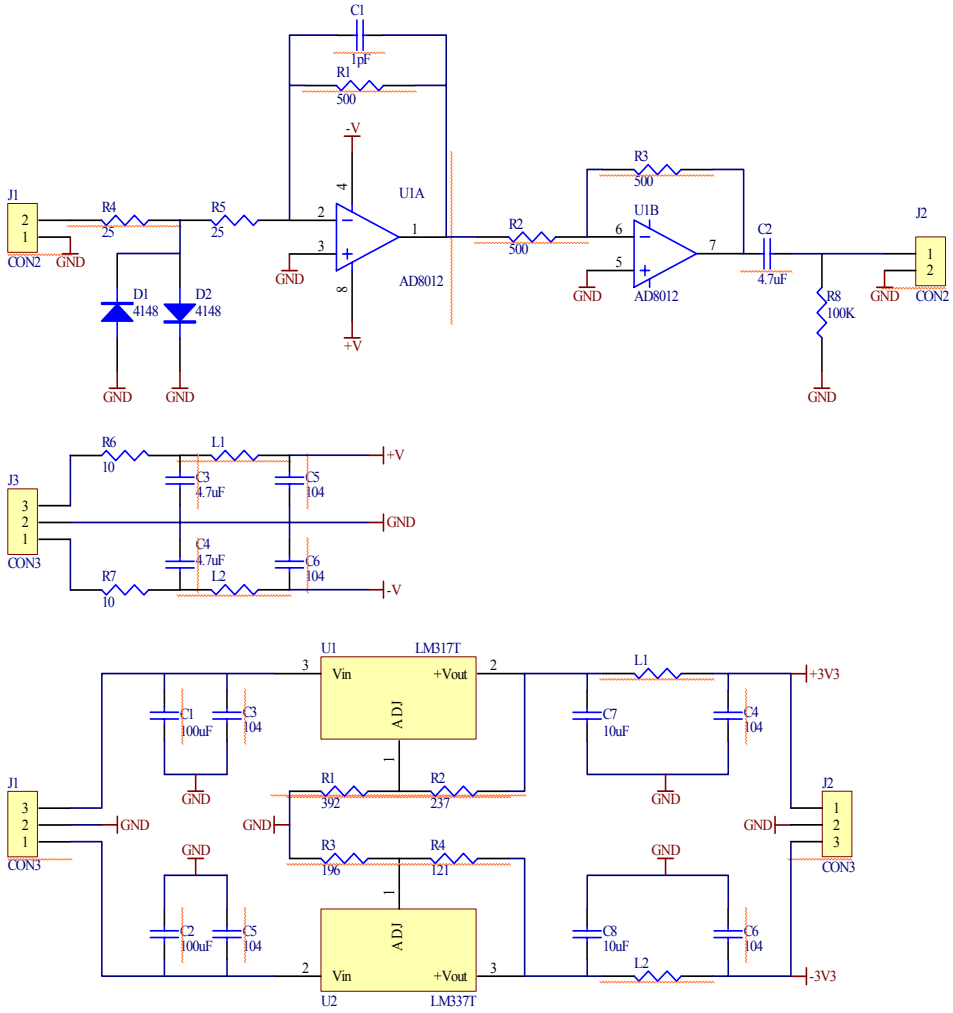

Figure 3.4 Schematic electronic diagram of preamplifier

3.3 Trigger

A schematic drawing of the trigger electronics is shown in Figure 3.5. Three fourfold coincidences are used to build the three possible two-tank coincidences, requiring each time a coincidence of the four phototube signals implied. The discriminator threshold and width were set at 17 mV and 40 ns respectively. An OR of the three two-tank coincidences makes the final

trigger. While the timing of each two-tank coincidence is defined by the latest of the four pulses contributing to it, the timing of the main trigger is instead defined by the earliest of the two-tank signals contributing to it.

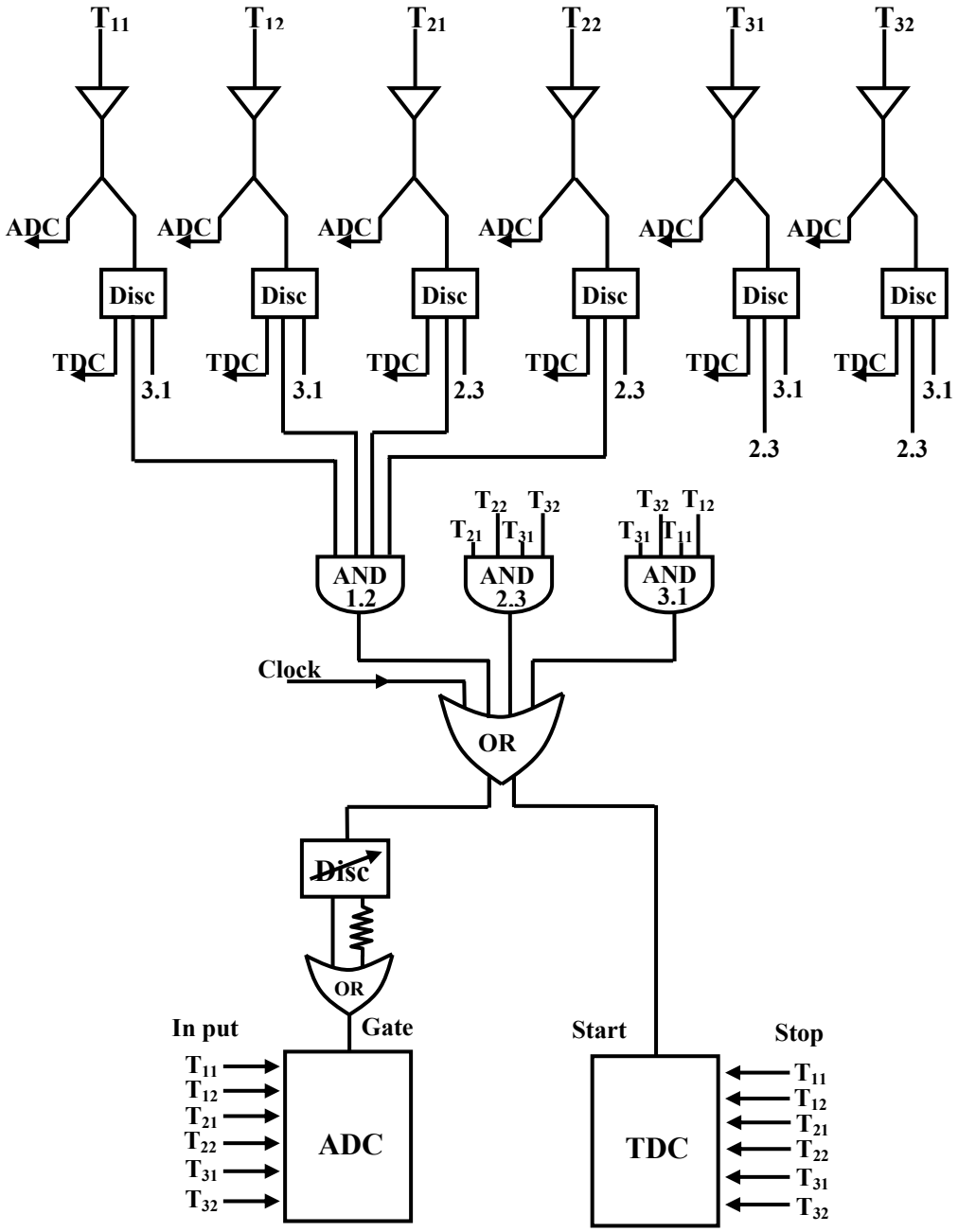

Figure 3.5: Diagram of trigger Electronics

As the main trigger is used as a gate to the ADC it is important to make sure that this gate is wide enough to accommodate the tube signals over a sufficient time range. The final trigger pulse was therefore sent to a discriminator that stretches its width to 100ns. For increased safety, and since the discriminator width could not exceed 100 ns, we ORed the discriminator output signal with itself after a 64 ns delay, thereby stretching it further by 64 ns additional as shown in the Figure 3.6. This signal is sent to the ADC gate and to the TDC start.

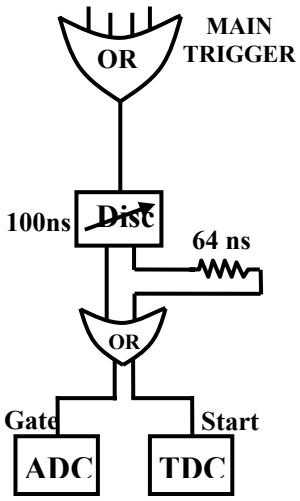

Figure 3.6 Diagram of ORed discriminator

3.4 Data acquisition

The data are collected into CAMAC units that are read out into the data acquisition PC using a CAMAC controller. The CAMAC units are a 12 input ADC LRS 2249A, a 8 input TDC LRS 2228A, and a 16 bit scaler of a four-scaler unit RRC 4CH 80MHz. The scaler records the output of a 10 kHz clock in order to measure the time separating successive triggers, and therefore the trigger rate (the distribution of this quantity is expected to be exponential with both the mean and rms values equal to the reciprocal of the rate). All units are reset at each trigger by a software command. The readout operation is started

by sending an appropriate signal (LAM=look at me) to the CAMAC controller whenever the ADC receives a gate, again using a software command. The program that organizes the CAMAC operations, DC-INT.C, is listed in appendix. The output of the program is a list of numbers that are made accessible to the main on-line monitoring program, EVENT.C, that is also listed in the appendix.

3.5 Adjustments and running in

3.5.1 Timing

A proper operation of the system requires an adequate timing of the various PMT signal pulses and a proper adjustment of the PMT high voltages (namely gains). In practice, one has to work by iteration in order to adjust, and later fine tune the various voltages and delays.

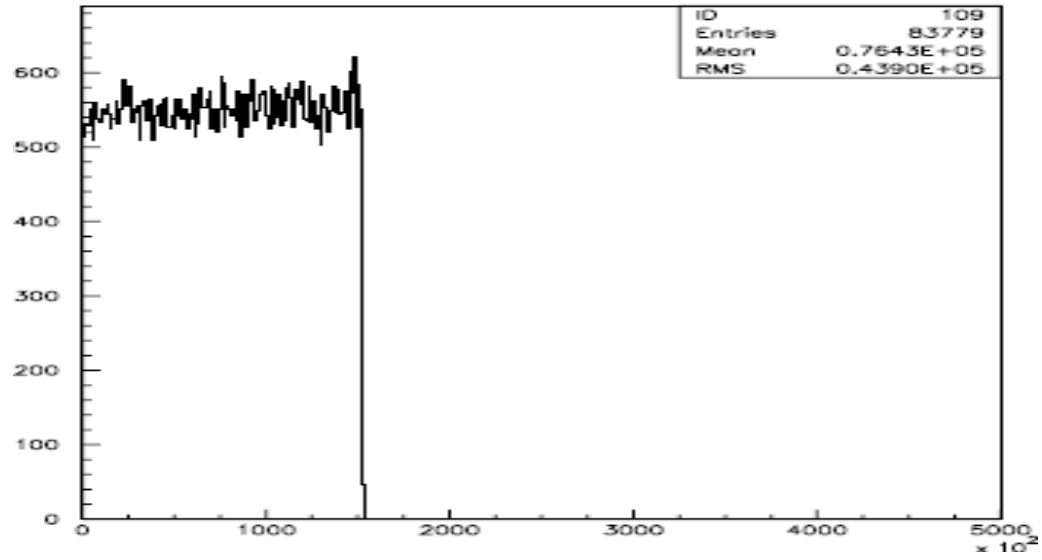

Figure 3.7 Trigger rates during the night and day. Each bin is 20 minutes long and the histogram covers two full days.

After having checked the system for light leaks (there were none, this was also checked more precisely later by comparing the night and day trigger rates, see Figure 3.7), the PMT high voltages were first set around 2kV in

order to crudely adjust the various delays. The discriminator thresholds were set to minimum, 17mV, which was found to be slightly over noise level. The relative timing of the two phototubes of a same tank was first tuned by scope, as the single tank rates are sufficient, and next by measuring delay curves for each of the three tanks (see Figure 3.8). The pulse height spectra recorded with these first settings were then used to group the six phototubes in three pairs, the members of each pair having similar gains, and to fix the high voltages as 2.20 kV (T11, T31), 2.10kV (T21, T22) and 1.90kV (T12 and T32).

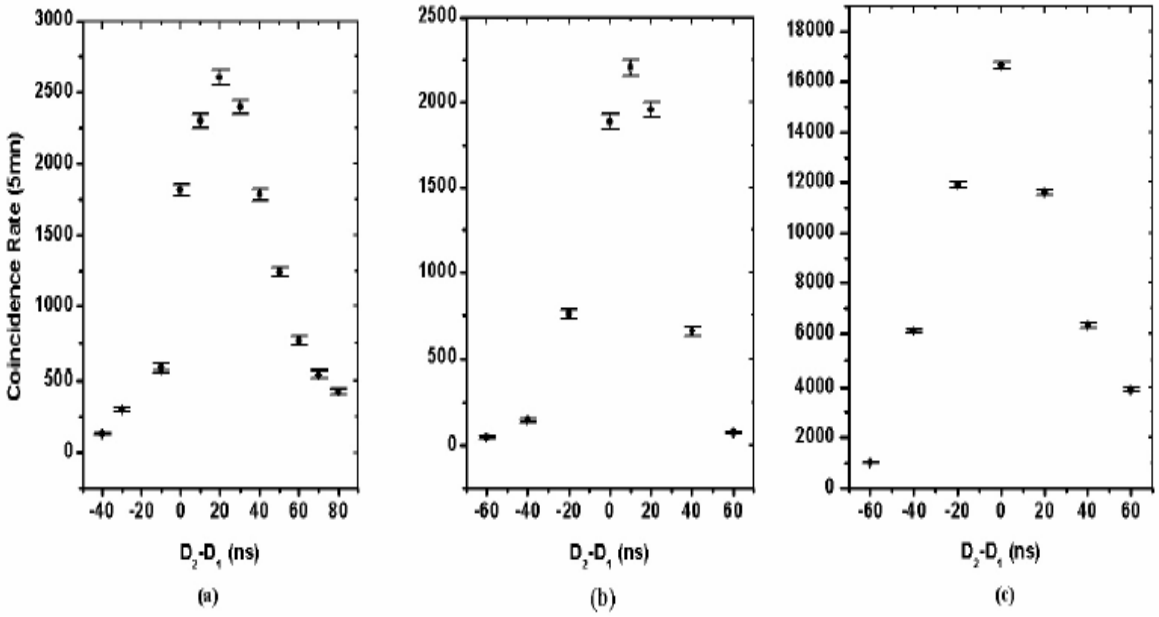

Figure 3.8: Delay curves between both PMT of each tank T_1, T_2, T_3 respectively (measured with a narrow pulse width)

The fine tuning of the delays was made by looking at the time difference of the signals of a same tank and at the time of arrival of a tank signal with respect to the trigger.

To do this we only considered tanks (flagged as OK) in which both phototubes have an ADC count between 10 and 800 channels and a TDC count also between 10 and 800 channels. The distributions of the TDC signals

are shown in Figure 3.9 for each of the PMT's in OK tanks. The calibration was made by introducing a fixed and known delay at the TDC start, with the result that 1ns corresponds to 5.4 channels. When a PMT defines the timing of the trigger, namely when it arrives latest in the four-fold coincidence that arrives first in the final OR, its TDC signal occurs at a fixed time, yielding the spikes in Figure 3.9.

The distribution of the time difference between the two phototubes of a same OK tank is shown in Figure 3.10 for tanks having the sum of the two PMT signals in excess of 200 channels in events having at least two OK tanks. The mean values of these distributions are respectively 4.7, -0.4, -1.9 channels for each of the three tanks, showing that the relative timing between the two PMTs of a same tank is good to better than 1 ns. However their rms is 16.1 ns on average, corresponding to an uncertainty on the time measurement $\sqrt{2}$ times smaller, namely $\Delta t = 11.4$ ns.

Some time slewing is expected. We recall that time slewing is the dependence of the TDC value on pulse height: if the pulse starting at time 0 reaches its maximal value $V_{\max}$ at time $T_{\max}$, the timing measured using a discriminator level V_{disc} will be nearly 0 when $V_{disc} << V_{\max}$ and $T_{\max}$ when V_{disc} reaches $V_{\max}$. In order to correct for this effect we study the dependence of $t_1 - t_2$ *over* $V_1 - V_2$ on PMT's 1 and 2 of a same tank in the above sample and find that the corrected value of the time measurement is $t' = t + 0.23V$ where t and V are measured in TDC and ADC channels respectively. As 1 TDC channel = 5.4 ns and 1 ADC channel = 0.5 mV, the time slewing correction amounts to 0.23 TDC channels per ADC channel, namely $0.23 \times \frac{5.4}{0.5} = 0.62 \frac{ns}{mV}$.

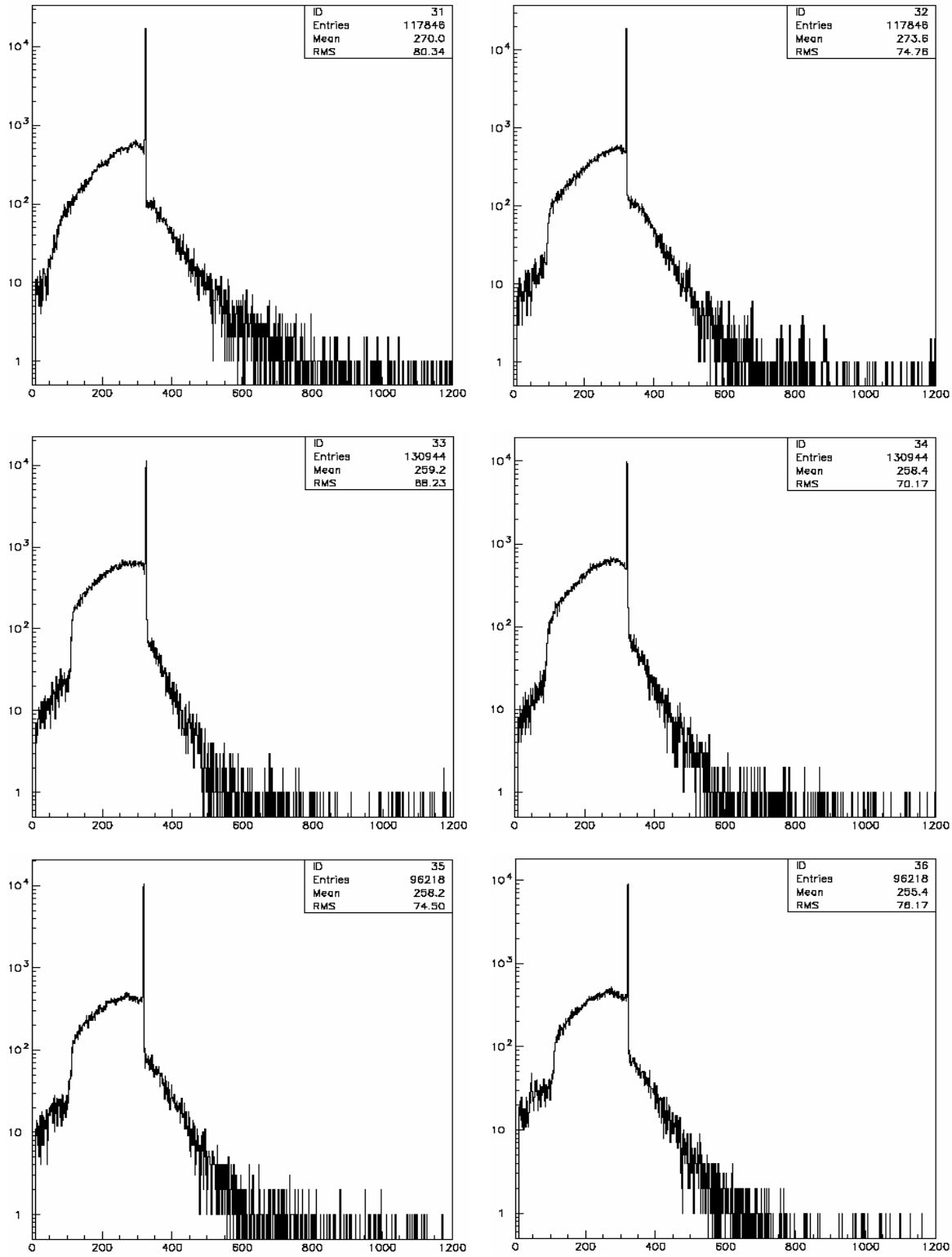

Figure 3.9 Distribution of TDC counts for each PMT of OK tanks

Figure 3.10 shows the t_1-t_2 distribution before and after correction. As expected, it becomes narrower after correction. The rms value is now 13.3 ns corresponding to Δt = 9.4 ns. This large value corresponds to a light path of 1.9 m in water, consistent with what can be expected from the tank geometry.

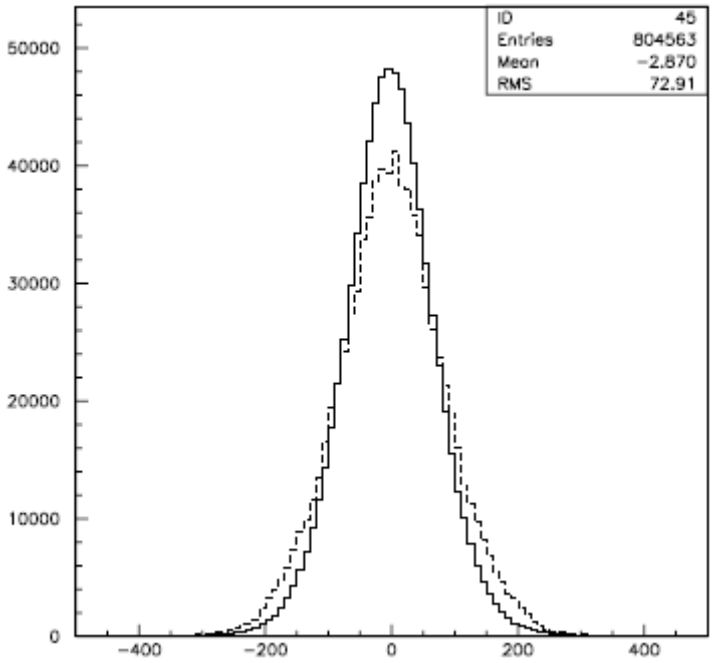

Figure 3.10 Time difference between two PMTs of the same tanks

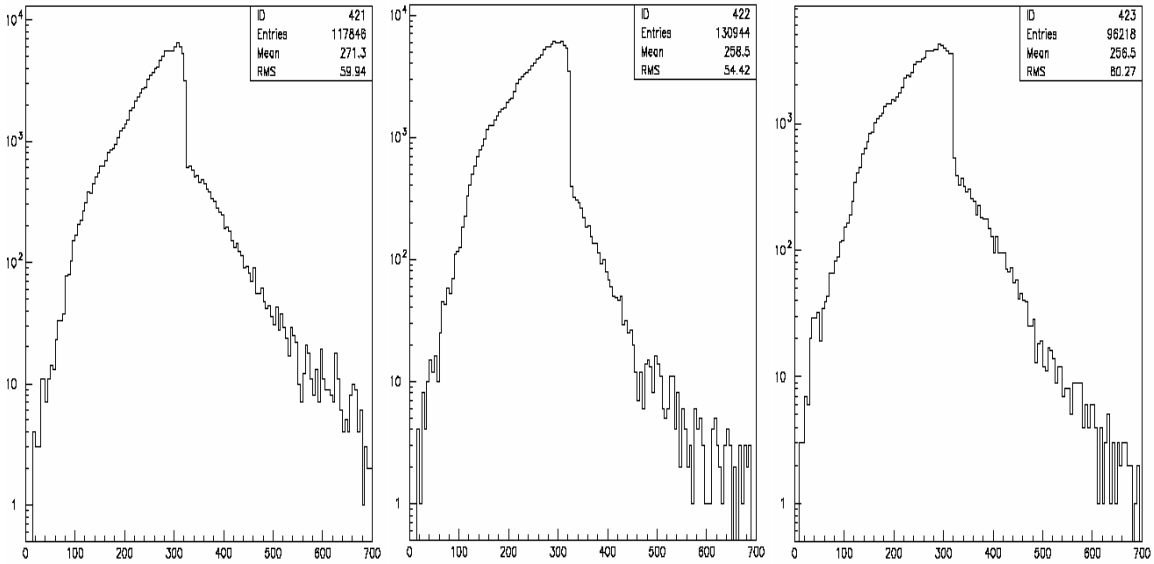

Figure 3.11 Time distributions of OK tanks

Figures 3.11 show the tank time distributions (before slew correction) of OK tanks where a “tank time” is defined as the average of the TDC signals of the two PMTs in that tank. We see here that the timing is good, although the signal in tank 1 arrives 2.6 ns later than that in tanks 2 or 3: the mean values are indeed 1.7, -0.7 and -1 ns when referred to their average.

At that stage, we define trigger tanks as OK tanks in which at least one of the two phototubes has its TDC signal within the 2ns wide spike of Figure 3.9 (TDC channels 315 to 325).

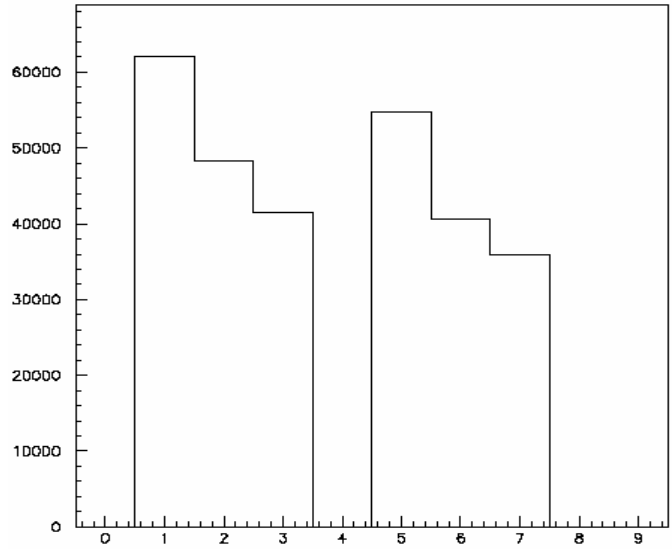

Figure 3.12 Trigger signals of each tank without requirement (left) or for single trigger tank events (right).

Figure 3.12 shows which tank is defined as a trigger tank either without further requirement (left part of the figure) or for events having one and only one trigger tank (right part of the figure). The grouping of the three values is sufficiently good for our purpose.

We then select events having one and only one trigger tank and look at the other (non trigger) OK tanks to evaluate their respective timings. The results are shown in Figure 3.13. With respect to their average value, the relative timings are 3.1, -1.4 and -1.8 ns respectively.

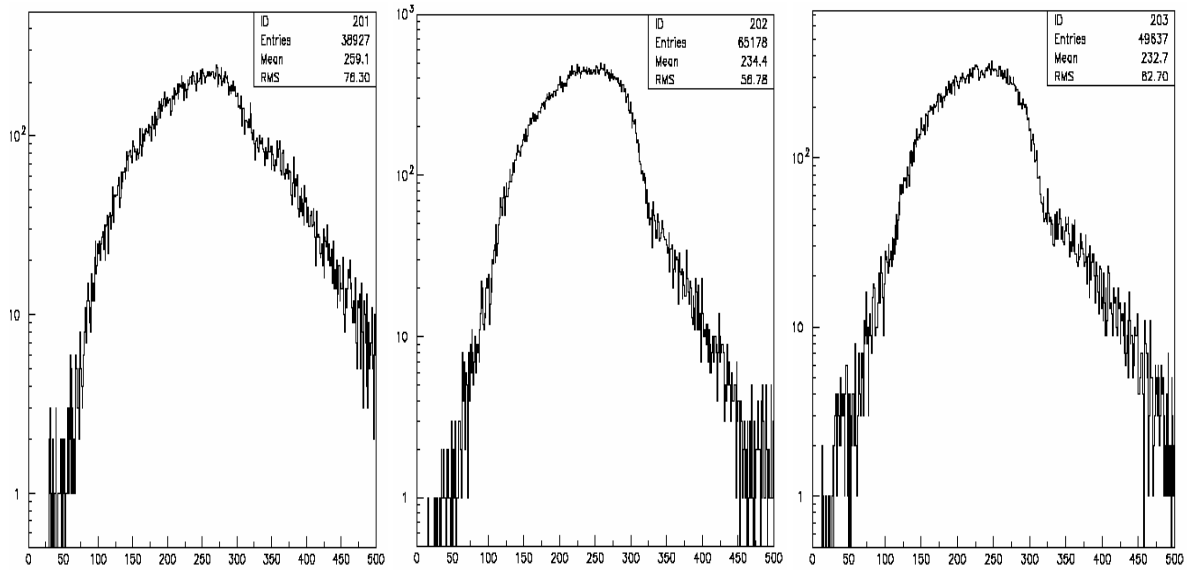

Figure 3.13 Time distributions for non-trigger OK tanks.

We checked the timing of the ADC gates by changing the gate delay by ± 8ns and checking that it made no effect on signals close to the relevant end of the gate.

3.5.2 Pulse heights

Important pedestals are present in the ADC signals: they need to be subtracted. To do this we measure the pedestals at the beginning of each run by sending 30 clock pulses into the main trigger. The average pulse height of each PMT over these 30 pulses is retained as pedestal. More precisely, in order to eliminate possible (but extremely unlikely) events where a real pulse falls into the clock trigger window, we retain only events having a very small deviation with respect to the mean. A typical distribution of pedestals measured in this way is shown in Figure 3.14.

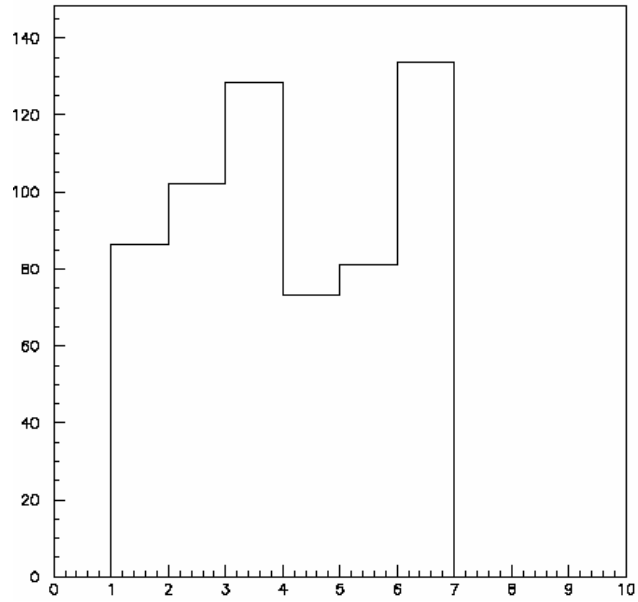

Figure 3.14 Pedestal distribution as measured at the beginning of a run

It is then possible to monitor their stability throughout the run as our trigger requires only two tanks to be on: the third tank will most of the time be off and give us a measure of the pedestal. This is done in Figure 3.15 for each of the six PMT's. To do this we have defined a large, medium and small tank as that having the largest, medium, or smallest tank pulse height. Figures 3.15 are plotted for the small tank defined in this way without further event selection. They show that over a whole run the pedestals are stable within ±14 channels but that, in some instances, we observe pedestal instabilities. In order to cope with these, we redefine pedestals every 20^{th} trigger, defining the new pedestal of a given tube as the minimum value of its signal in the past twenty events. Figures 3.16 show the distribution of the pedestals defined in this way over a large series of runs including runs where they were jumping between two different values. From these plots we find that the pedestals are now defined to within ±3.3 channels.

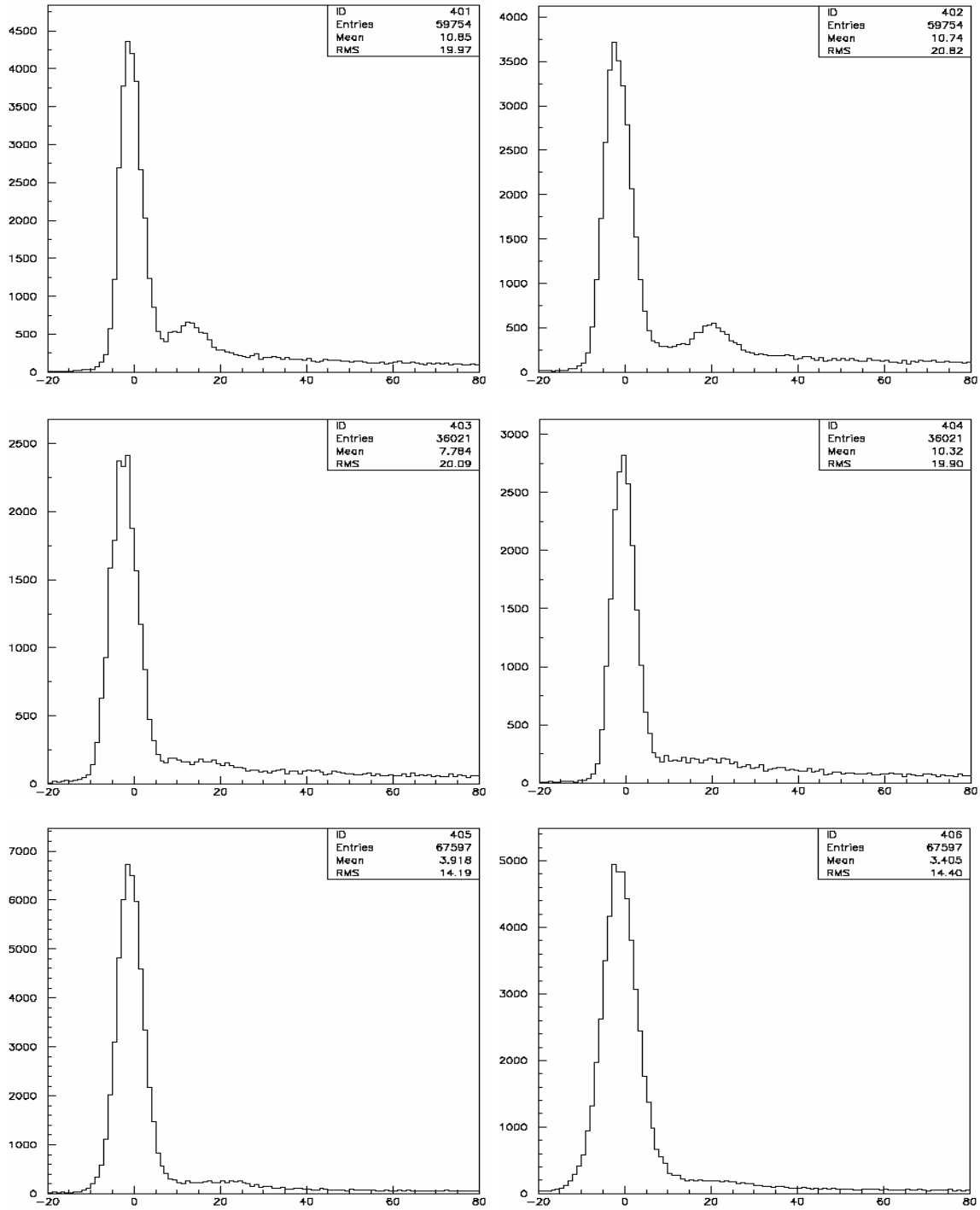

Figure 3.15 Pulse height distributions of the phototubes of the tank having the smallest mean pulse height showing clear pedestal peaks centered at 0 and having rms values of less than 14 channels typically. The first two histograms give evidence for a pedestal shift during the run

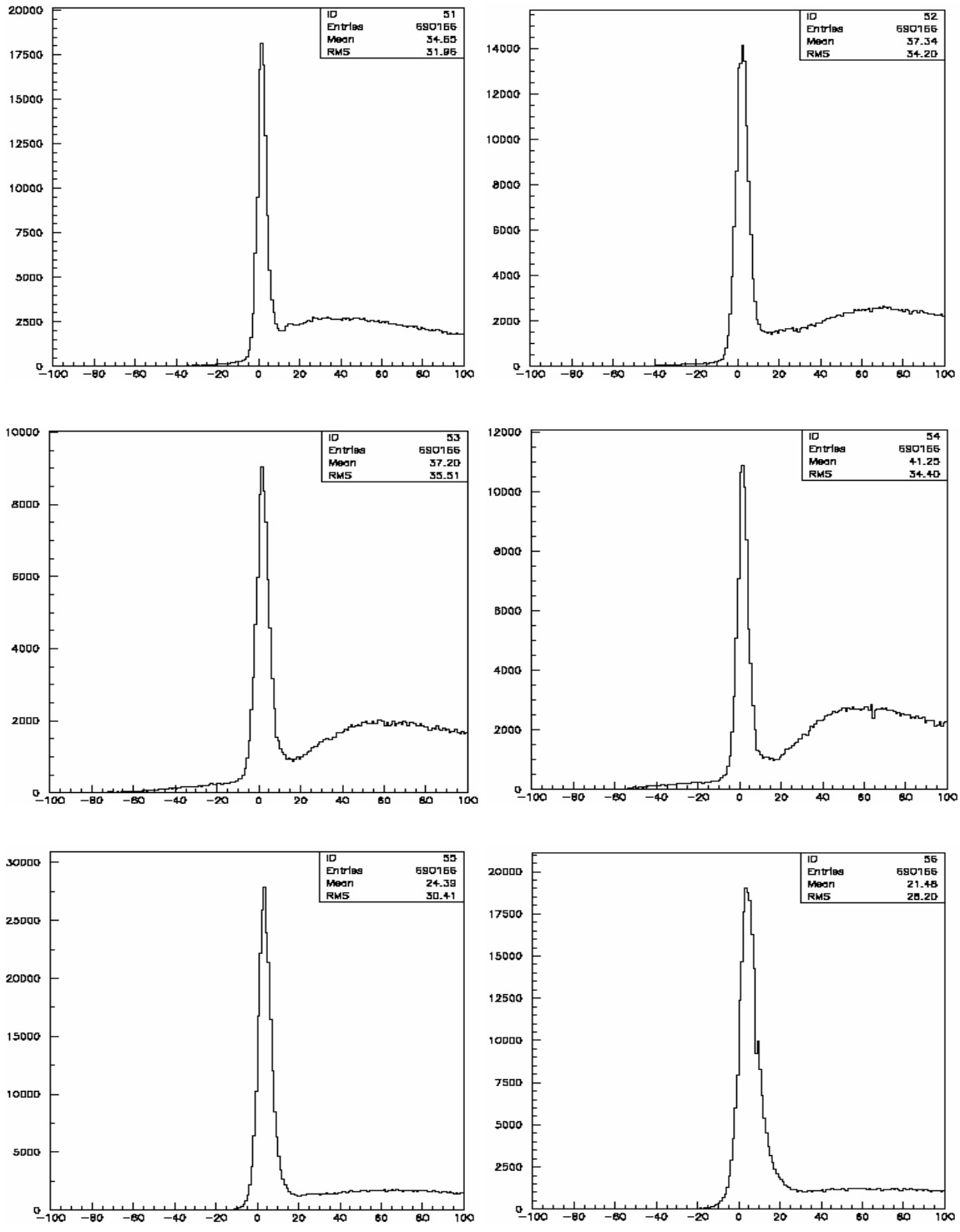

Figure 3.16 Distributions of pedestals corrected after every 20^{th} event.

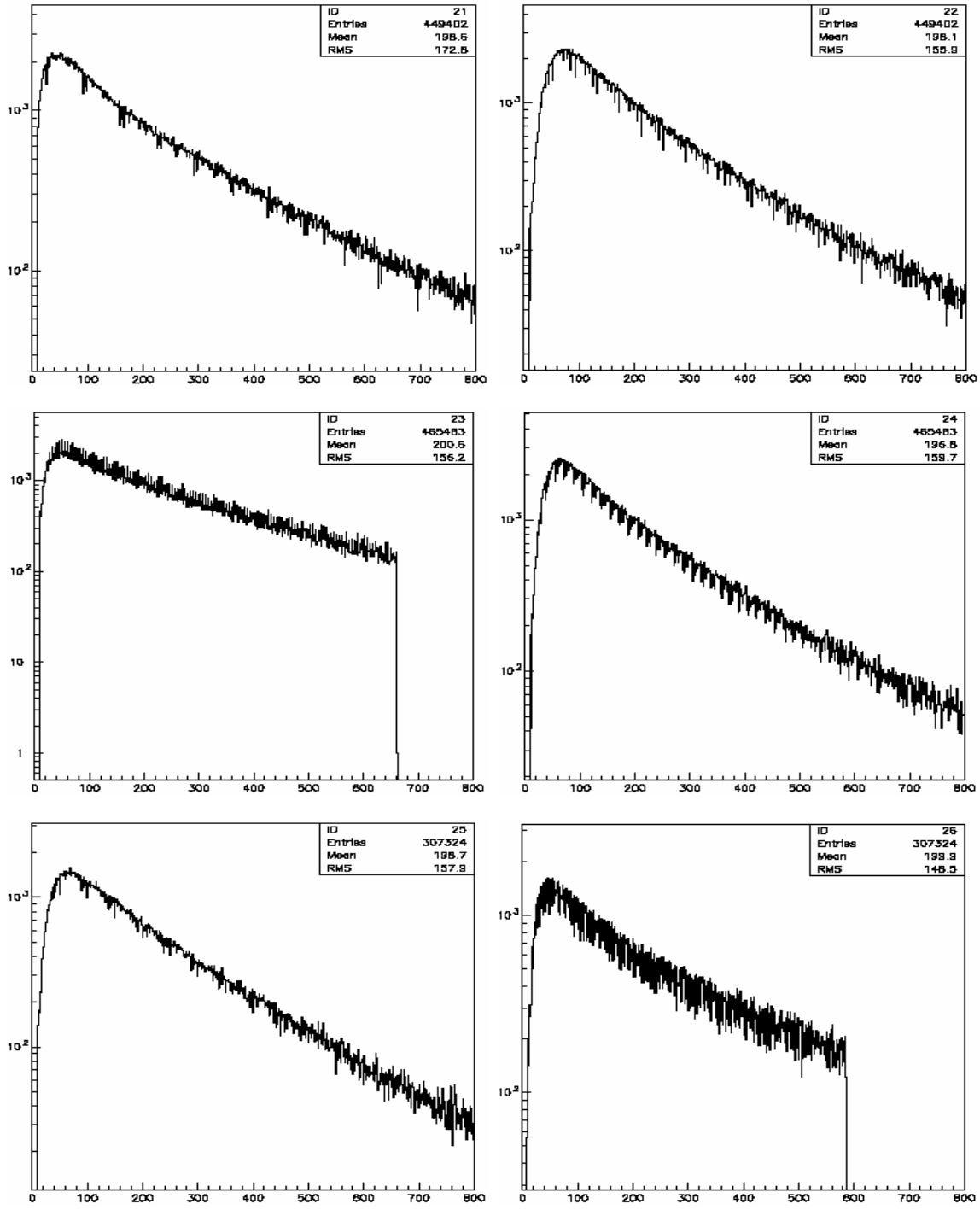

Figure 3.17 PMT pulse height distribution for OK tanks

The pedestal subtracted pulse height distributions of phototubes in OK tanks are shown in Figure 3.17. They show the effect of the trigger (discriminator threshold) at low pulse heights (however the figure includes

non-trigger tanks: to see clearly the trigger threshold, 17 mV corresponding to some 30 ADC channels, one has to look at trigger tank distributions exclusively). At higher pulse heights, they also show the effect of saturation (not visible on the figure). In order to be free of saturation effects, we also took data in which the PMT's signals were sent directly to the ADC without prior amplification. They will not be discussed here.

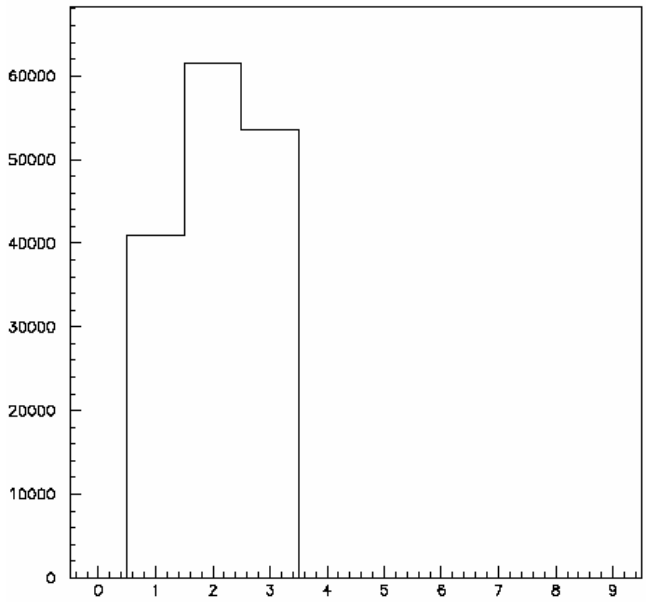

Figure 3.18 Histogram showing tanks having the highest pulse height

Figure 3.18 shows which tank has the largest signal : it is tank 1, 2, and 3 respectively 26%, 39% and 35% of the time, again showing that our choice of high voltages is reasonable. Tank pulse heights are defined as the average pulse height of the PMT's of that tank. Their distributions for OK tanks are shown in Figure 3.19. The bumps on these distributions correspond to events where one PMT saturates and the other not. Eliminating such events gives the distributions shown on the same figures (lower curves), showing that indeed the bump has disappeared.

Using events in which at least two tanks are flagged as OK, we correct for the different gains of each phototube by looking at the distribution of the

asymmetries in each tank, $\frac{1}{2}(V_1 - V_2)/(V_1 + V_2)$ for events having $V_1 + V_2 > 200$ channels and making them to cancel on average. The corrected asymmetry distributions obtained for $V_1 + V_2 > 200$ and 800 channels respectively are shown on Figure 3.20. Their rms values are 0.22 and 0.16. For uncorrelated uncertainties ΔV_1 and ΔV_2 on V_1 and V_2 we expect an rms asymmetry of the order of $\sqrt{2}\,\frac{\Delta V}{V}$: we estimate from this $\frac{\Delta V}{V} = 16\,\%$ and 11% for the 200 and 800 channels cuts respectively (corresponding to 100 mV and 400 mV). Table 3.1 lists the correction factors.

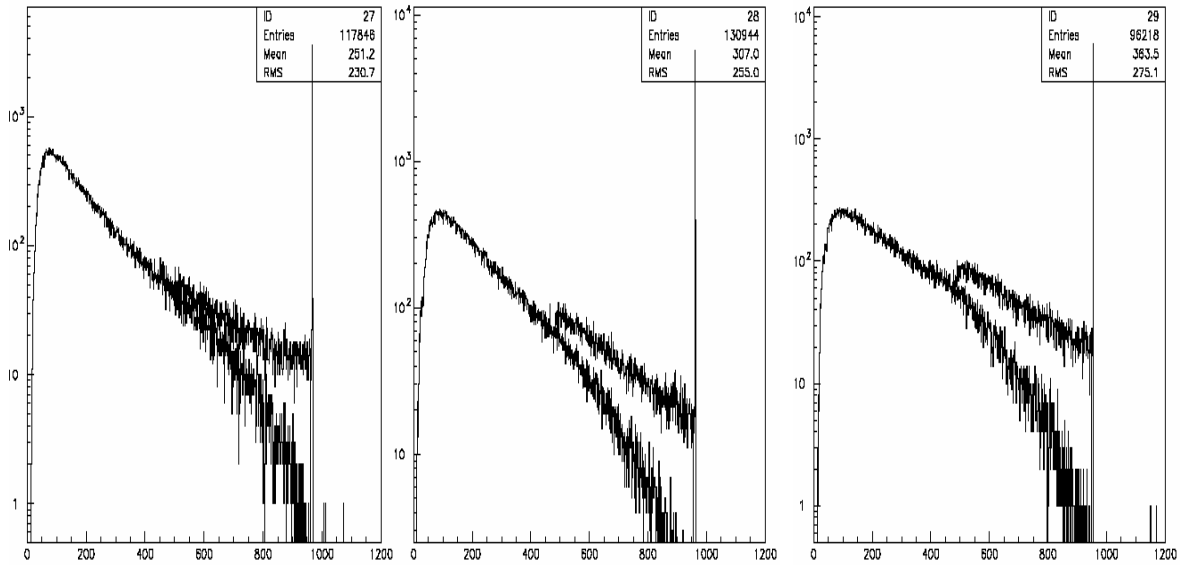

Figure 3.19 Tank pulse height distributions for OK tanks (see text).

Table 3.1 Gain correction

	ph T_{11}	ph T_{12}	ph T_{21}	ph T_{22}	ph T_{31}	ph T_{31}
PMT gain	1.04	.94	1.16	.95	.97	1.23

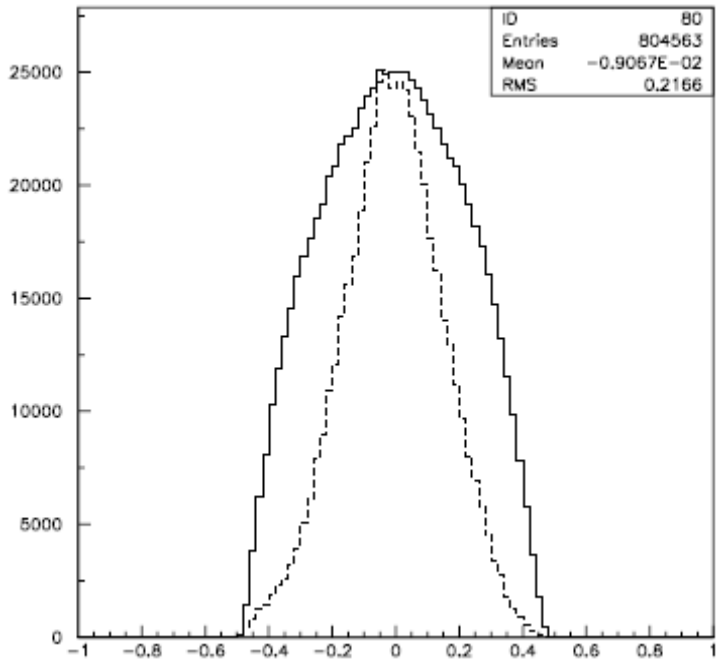

Figure 3.20 Distribution with the cut at 800 has been scaled up by a factor 5

Finally Figure 3.21 shows the distribution of the sum of the three tank signals for events having three OK tanks.

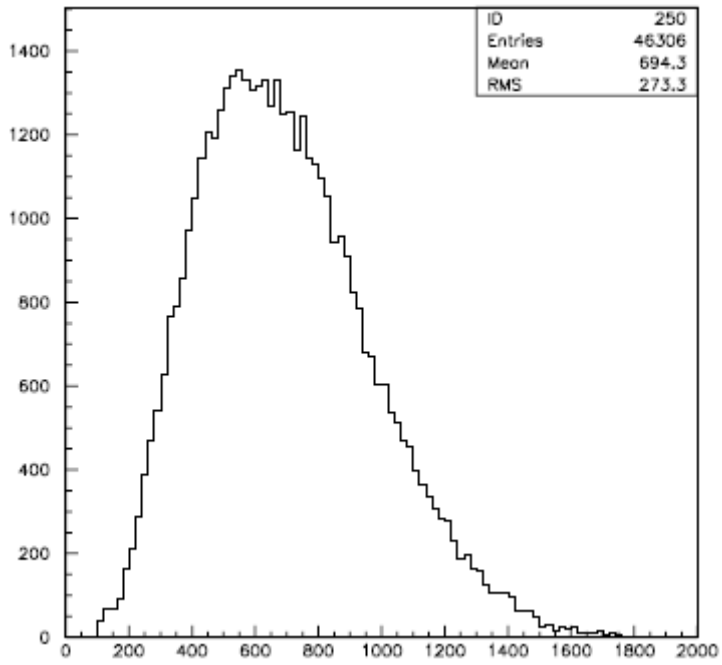

Figure 3.21 Distribution of three OK tank signals

3.5.3 Rates

The accidental rate was measured and found negligible. The measurement was made by delaying the phototube that has the highest single rate, T21, and excluding from the trigger coincidence 1.3 to which it does not contribute. A 1 μs delay was introduced using a timing unit (see Figure 3.22) and data were collected for a period of 21 hours. Five random events were recorded, corresponding to a rate of 7.5 10^{-5} Hz. The relevant single rates were 850 Hz for T21 and 0.88 Hz for the OR of (T22 and T31 and T32) and (T22 and T11 and T12). Hence an effective resolution of the coincidence $\Delta t = \frac{7.5.10^{-5}}{0.88 * 850} = 100ns$, in perfect agreement with expectation.

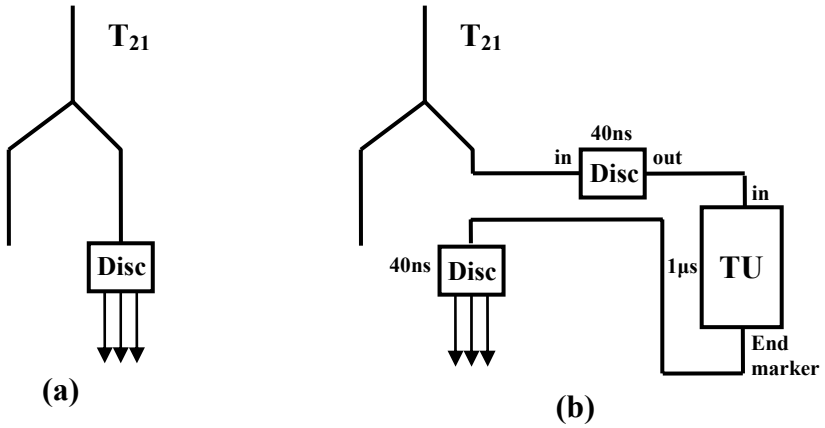

Figure 3.22: Schematic of accidental

The distribution of the time separating two successive triggers was usually found exponential, as expected for random events, with equal mean and rms values, corresponding to a trigger rate of 0.54 Hz (Figure 3.23). Note that when the time exceeds some 6.6 seconds, the scaler overflows and starts counting from 0 again. This changes slightly the mean and rms values which would correspond, if this overflow effect were ignored, to a mean time of 0.56 Hz. However, the value 0.54 Hz, obtained from the slope of the distribution in Figure 3.2.3, is not affected by the overflow effect.

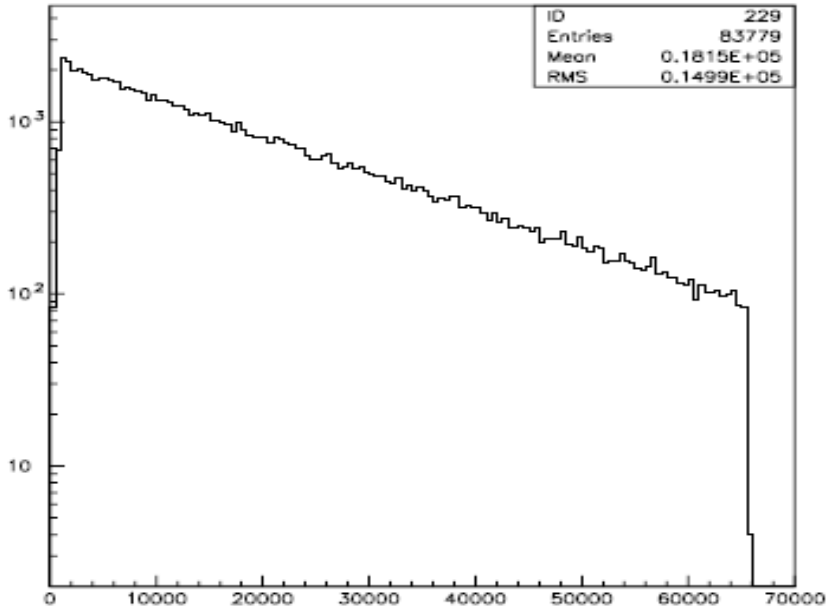

Figure 3.23 Distribution of the time between triggers. One bin is 10^{-4} second wide and the mean value of the time between triggers measured from the slope of the curve is .54 Hz.

In summary typical rates were 7.5 Hz for single tanks (two PMT coincidences), 0.3 Hz for two-tank coincidences and .015 Hz for three tank coincidences, well above the expectation for uncorrelated tanks: 6 10^{-6} Hz and 4 10^{-12} Hz respectively. This gives clear evidence in favor of extensive air showers as was first discovered by Pierre Auger.

For events having three OK tanks (as shown in Figure 3.21) it is possible to reconstruct the direction from which the shower is coming using relations:

$$\begin{cases} t_1 = X_1 \sin\theta\cos\varphi + Y_1 \sin\theta\sin\varphi + t_0 \\ t_2 = X_2 \sin\theta\cos\varphi + Y_2 \sin\theta\sin\varphi + t_0 \\ t_3 = X_3 \sin\theta\cos\varphi + Y_3 \sin\theta\sin\varphi + t_0 \end{cases}$$

where θ and φ are the zenith angle and the azimuth of the direction of arrival and where t_1, t_2, t_3 are the three tank times as defined earlier, (X_1, Y_1), (X_2, Y_2), (X_3, Y_3) being the coordinates of each tank and t_0 the event time.

Figure 3.24 shows the two dimensional distribution of the horizontal projection of the unit vector directed along the shower axis, $u_x = \sin\theta.\cos\varphi$ and $u_y = \sin\theta.\sin\varphi$.

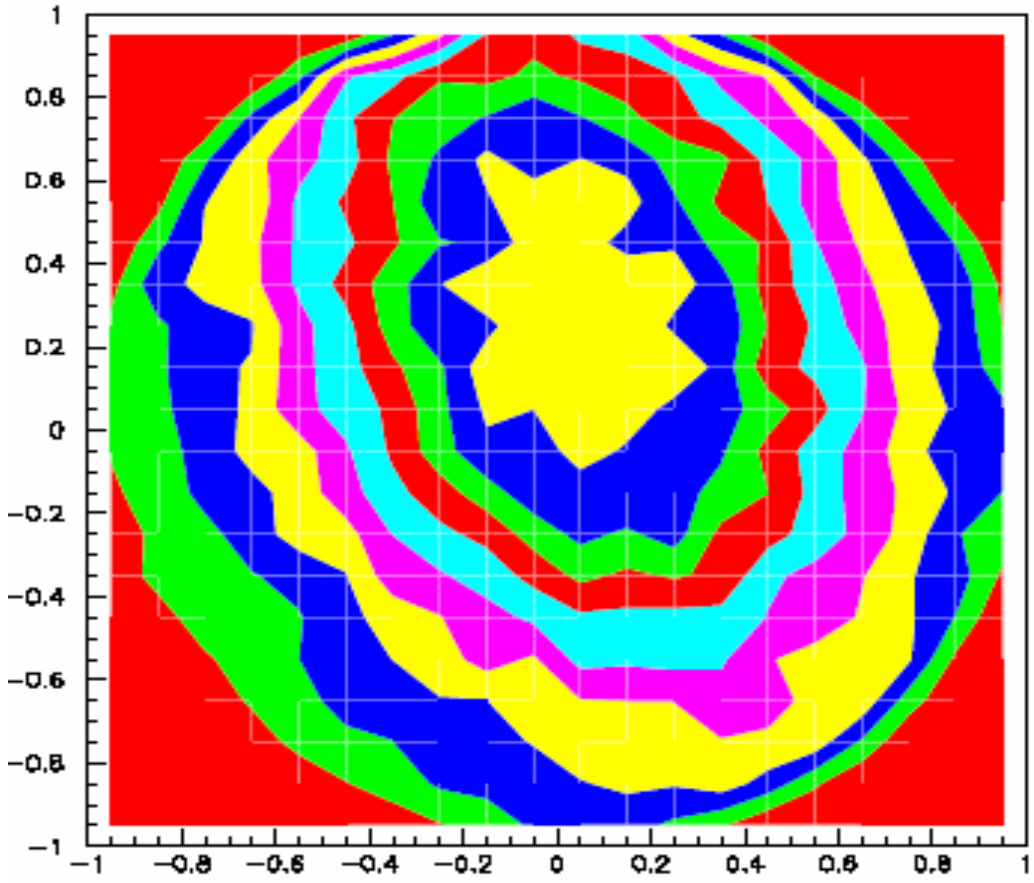

Figure 3.24 Distribution of the horizontal projection of the unit vector directed along the shower axis

Chapter 4

Summary and perspectives

The present work summarizes a series of hardware contributions made to the VATLY detectors and to which I gave major, and often exclusive contributions. It concerns both the large Cherenkov counter that is a replica of those used in the surface detector of the Pierre Auger Observatory and three additional smaller counters, also water Cherenkov detectors, which have been installed around it in order to provide a trigger on extensive air showers.

The work on the large Auger-like counter included studies of after-pulsing and a major refurbishing of the detector. The latter included the installation of new photomultiplier tubes and of their associated power supplies and front-end electronics, a complete recoating of the counter walls using aluminized mylar and the installation of a new additional filtering system meant to improve the purity of the water by a factor 10 or so. The refurbishing is now completed and the system has been successfully tested with a scintillator plate replacing the water. The tank is presently being filled and should be ready for operation with water by the end of October. The amount of light collected will hopefully be significantly larger than before and approach that achieved in the PAO.

The work on the smaller tanks included the design of the system, its construction and assembly and its testing and running-in. These various phases have been described in detail and have shown that the performance of the system was satisfactory and adequate to its purpose of serving as a trigger on extensive air showers for the large Auger-like counter. A first account of

the operation of the full system was outside the scope of the present thesis work and will be the subject of the master thesis of a colleague of mine [16].

Continuation of this work will proceed along two different lines: one to study the details of the shower data collected with these detectors and one to perform a number of careful studies which are useful to the Auger collaboration in order to better understand the detailed behavior of the main Cherenkov counter. The latter include a detailed study of the photomultiplier response: single photoelectron spectrum, uniformity of the photocathode, possible after-pulsing, geometric effects relevant to the timing and efficiency of the photoelectron acceleration process, etc. I will spend the months of November and December in Orsay (Institut de Physique Nucléaire) near Paris, in the group of Professor Tiina Suomijärvi, where there is much expertise on the photomultiplier tubes and associated electronics. I hope this way be better prepared to tackle these additional studies and to be able to work in collaboration with the Orsay team, possibly toward a PhD thesis under joint supervision of Hanoi and Orsay.

References

1. G.T. Zatsepin and V.A. Kuzmin(1966), JETP Lett. **4** 78.

   K.Greisen(1966), Phys. Rev. Lett. **16** 748.

2. R.M. Baltrusaitis et al.(2004), Nucl. Instr. Meth. A 523, 50.

   D.J Bird,. et al. 1993, ICRC, **2** 34.

   D.J. Bird, et al. (1995), Astrophys. J. **441** 144.

   G. Davidson and R. Oneil (1964), J. Chem. Phys . **41** 3946

3. N. Hayashida et al. (1994) , Phys. Rev. Letters **73** 3491.

   S. Yoshida et al. (1995), Astropart. Phys. **3** 105.

   M. Takeda et al. (1998), Phys. Rev. Lett. **81** 1163.
   M. Takeda, et al. (1999), in Proceedings of the 26th International Cosmic Ray Conference, Vol. **3** 252.

4. The Pierre Auger Observatory Design Report, The Auger Collaboration, 2nd Edition, Fermi Laboratory, November 1996, Revised March 1997.
   http://www.auger.org/admin/DesignReport/index.html

5. J.W. Cronin (2003), Proceedings of the TAUP meeting, Seattle, September.
6. M. Nagano and A.A. Watson (2000), Rev. Mod. Phys. **72** 689.
7. A. M. Hillas (1984), Annual Review Astron. Astrophys. **22** 425
8. "The Pierre Auger Observatory Progress and First Results", Pierre Auger Collaboration, Proceedings – 29th ICRC, Pune, India (2005).
9. J. Abraham, et al. (2004), Pierre Auger Collaboration, Nucl. Inst. Meth. A523 50.

10. The Pierre Auger Project, Technical Design Report, The Auger Collaboration, March 2004.
    http://tdpc01.fnal.gov/auger/org/tdr/index.html

11. M. A. Lawrence, R. J. O. Reid, A. A. Watson (2000), J. Phys. G. **17** 773.

12. M. Aglietta et al. (2005), Proc. Of 29th ICRC, Pune, 7, 83.

    X. Bertou (2003), Proceedings of the 28th ICRC (Tsukuba).

    X. Bertou, et al (2006), Preprint submitted to Elsevier Science.

13. P.N. Dinh et al. (2002), Nucl. Phys., 627B 29.
    P.N. Dinh et al(2003)., Nucl. Phys. 661B 3.
    P.N.Diep et al. (2003), Com. Phys. Vietnam **14**, 56.

14. P.T.T. Nhung (2006), Master thesis.

15. P.N. Dong (2004), After pulsing, VATLY Internal Note Nr. 12.

16. N.T. Thao, Master thesis, in preparation.

Appendices

1. DC_INT.C

```
/*--------------------------------------------------------------------------*/
/* System :   VATLY Laboratory                                              */
/* File   :   dc_int.c                                                      */
/* Description: Cerenkov - Multi event acquisition                          */
/*--------------------------------------------------------------------------*/
#include "camack.c"
/* ADC 12ch  LSR 2249A Fr=0 Fc=9 Ac=11  */
#define ADC_N1        18
#define ADC_N2        21
#define TDC1           9
#define TDC2          12
#define SCL1          14

static long  loop=0,data;
static int   stat;
static void dc_int_init(),dc_int_start(),dc_int_stop(),dc_int_clear();
       void cleanup_module();
/*-------------------------------------------------------------------------
*/
/* COM> start, stop, clear    functions                                     */
/*-------------------------------------------------------------------------
*/

static void dc_int_init(){
    dc_int_start();
}
static void dc_int_start(){
 /*LAM Ae1=11 Fe1=26 Ad1=11 Fd1=24 Ac1=11 Fc1=10*/
  dc_int_clear();
  camac_NAF(ADC_N1,11,10);  /* clear  LAM   */
  camac_NAF(ADC_N1,11,26);  /* enable LAM   */

  camac_NAF(ADC_N1,11,9); /*clear ADC*/
  camac_NAF(ADC_N2,11,9); /*clear ADC*/

  camac_NAF(TDC1,0,9); /*clear TDC*/
  camac_NAF(TDC1,1,9);
  camac_NAF(TDC1,2,9);
  camac_NAF(TDC1,3,9);
  camac_NAF(TDC1,4,9);
  camac_NAF(TDC1,5,9);
  camac_NAF(TDC1,6,9);
  camac_NAF(TDC1,7,9);

  camac_NAF(TDC2,0,9); /*clear TDC*/
  camac_NAF(TDC2,1,9);
  camac_NAF(TDC2,2,9);
  camac_NAF(TDC2,3,9);
  camac_NAF(TDC2,4,9);
  camac_NAF(TDC2,5,9);
  camac_NAF(TDC2,6,9);
```

```
  camac_NAF(TDC2,7,9);

  camac_NAF(SCL1,0,9); /*clear SCL*/
  camac_NAF(SCL1,1,9);
  camac_NAF(SCL1,2,9);
  camac_NAF(SCL1,3,9);

}
static void dc_int_stop(){
  camac_NAF(ADC_N1,11,24);  /* disable LAM  */
}
static void dc_int_clear(){
  camac_NAF(ADC_N1,11,9);       /* ADC_N1 clear */
  camac_NAF(ADC_N1,11,10);      /* clear  LAM  */
  camac_NAF(ADC_N2,11,9);       /* ADC_N2 clear */
  camac_NAF(ADC_N2,11,10);      /* clear  LAM  */
}
static int dc_int(unsigned short buf[]){
static long   j;
     loop++;
     if((j = inl(BASE_ADDRESS+4)) == 0){
       if(loop > 100)   cleanup_module();
       if(dc_int_flag == 0) outl(0,BASE_ADDRESS);
       else                 outl(0,BASE_ADDRESS);
       return(-1);  /* reset interrupt from crate controller */
     }
      buf[0]=45;
/* ADC 1*/
         camac_NAF(ADC_N1,0,0); buf[1]= camac_read16();
         camac_NAF(ADC_N1,1,0); buf[2]= camac_read16();
         camac_NAF(ADC_N1,2,0); buf[3]= camac_read16();
         camac_NAF(ADC_N1,3,0); buf[4]= camac_read16();
         camac_NAF(ADC_N1,4,0); buf[5]= camac_read16();
         camac_NAF(ADC_N1,5,0); buf[6]= camac_read16();
         camac_NAF(ADC_N1,6,0); buf[7]= camac_read16();
         camac_NAF(ADC_N1,7,0); buf[8]= camac_read16();
         camac_NAF(ADC_N1,8,0); buf[9]= camac_read16();
         camac_NAF(ADC_N1,9,0); buf[10]= camac_read16();
         camac_NAF(ADC_N1,10,0); buf[11]= camac_read16();
         camac_NAF(ADC_N1,11,0); buf[12]= camac_read16();
/*ADC 2 */
         camac_NAF(ADC_N2,0,0); buf[13]= camac_read16();
         camac_NAF(ADC_N2,1,0); buf[14]= camac_read16();
         camac_NAF(ADC_N2,2,0); buf[15]= camac_read16();
         camac_NAF(ADC_N2,3,0); buf[16]= camac_read16();
         camac_NAF(ADC_N2,4,0); buf[17]= camac_read16();
         camac_NAF(ADC_N2,5,0); buf[18]= camac_read16();
         camac_NAF(ADC_N2,6,0); buf[19]= camac_read16();
         camac_NAF(ADC_N2,7,0); buf[20]= camac_read16();
         camac_NAF(ADC_N2,8,0); buf[21]= camac_read16();
         camac_NAF(ADC_N2,9,0); buf[22]= camac_read16();
         camac_NAF(ADC_N2,10,0); buf[23]= camac_read16();
         camac_NAF(ADC_N2,11,0); buf[24]= camac_read16();

/* TDC1, 8channels */
         camac_NAF(TDC1,0,0);  buf[25]=  camac_read16();
         camac_NAF(TDC1,1,0);  buf[26]=  camac_read16();
         camac_NAF(TDC1,2,0);  buf[27]=  camac_read16();
```

```
        camac_NAF(TDC1,3,0);  buf[28]=  camac_read16();
        camac_NAF(TDC1,4,0);  buf[29]=  camac_read16();
        camac_NAF(TDC1,5,0);  buf[30]=  camac_read16();
        camac_NAF(TDC1,6,0);  buf[31]=  camac_read16();
        camac_NAF(TDC1,7,0);  buf[32]=  camac_read16();
/* TDC2, 8channels */
        camac_NAF(TDC2,0,0);  buf[33]=  camac_read16();
        camac_NAF(TDC2,1,0);  buf[34]=  camac_read16();
        camac_NAF(TDC2,2,0);  buf[35]=  camac_read16();
        camac_NAF(TDC2,3,0);  buf[36]=  camac_read16();
        camac_NAF(TDC2,4,0);  buf[37]=  camac_read16();
        camac_NAF(TDC2,5,0);  buf[38]=  camac_read16();
        camac_NAF(TDC2,6,0);  buf[39]=  camac_read16();
         camac_NAF(TDC2,7,0);  buf[40]=  camac_read16();
/* SCL1, 4scalers */
     camac_NAF(SCL1,0,0);  buf[41]=  camac_read16();
     camac_NAF(SCL1,1,0);  buf[42]=  camac_read16();
     camac_NAF(SCL1,2,0);  buf[43]=  camac_read16();
     camac_NAF(SCL1,3,0);  buf[44]=  camac_read16();

                camac_NAF(ADC_N1,11,9);
                camac_NAF(ADC_N2,11,9);
                 camac_NAF(TDC1,0,9);
                camac_NAF(TDC1,1,9);
                camac_NAF(TDC1,2,9);
                camac_NAF(TDC1,3,9);
                 camac_NAF(TDC1,4,9);
                camac_NAF(TDC1,5,9);
                camac_NAF(TDC1,6,9);
                camac_NAF(TDC1,7,9);

                 camac_NAF(TDC2,0,9);
                camac_NAF(TDC2,1,9);
                camac_NAF(TDC2,2,9);
                camac_NAF(TDC2,3,9);
                 camac_NAF(TDC2,4,9);
                camac_NAF(TDC2,5,9);
                camac_NAF(TDC2,6,9);
                camac_NAF(TDC2,7,9);

          camac_NAF(SCL1,0,9);
          camac_NAF(SCL1,1,9);
          camac_NAF(SCL1,2,9);
          camac_NAF(SCL1,3,9);

return(0);
}
```

2. EVENT.C

```
/*--------------------------------------------------------------------*/
/* System :     Hanoi Auger Group                                     */
/* File   :   event.c                                                 */
/* Description:    On-line data taking small tanks 21/12/05           */
/* General framework                                                  */
/*--------------------------------------------------------------------*/

#include "/home/cern/pro/include/cfortran/cfortran.h" /* C -> FORT
conversion */
#include "/home/cern/pro/include/cfortran/hbook.h"  /* HBook Library
(FORT) */
#include <math.h>
#define HBOOK_SIZE 200000
#include "blocker.h"

//struct SHM_CC7700 *shmp;

void analyze_( name, data )
char*               name;   /* PAW-HBook global_sec ID
"ONLINE"/"OFFLINE"  */
unsigned short int data[]; /* one event raw data data[0]=event word
length*/
{
  static int loop=0;
  static unsigned long int nhung=0,goodpairs=0;
  int i,j,k,l,okall,bit1,bit2;
  int
anhem[7]={0,2,1,4,3,6,5},ok[7],trig[4],jj[4]={0,2,3,1},kk[4]={0,3,1,2};
  float alpha,beta,phi,costh,sinth,ux,uy,ux30,sctest,dummy[14],ttnow;
  static float
ttotal=0.,ttotal0=0.,ttotal1=0.,ttotal2=0.,scold=0.,ttold=0.;
  static float xx[4]={0.,445.,496.,-396.},yy[4]={0.,15.,-448.,-460.};
  static float
ttank[4],phtank[4],pmean[7]={0.,177.,183.,226.,168.,178.,242.};
  static int large,small,medium,nped=0,oktank[4];
  static float
ph[7],time[7],scaler[5],phall,phpair,det0,pi=3.14159,conv=5.59;
  float satur[7];

//*********************************************************************
// don't set flag = 1 unless you are sure to know what you are doing
// static int flag=0;
//*********************************************************************
  static float ped[7]={0.,0.,0.,0.,0.,0.,0.};
  static float gain[7]={1.,1.,1.,1.,1.,1.,1.};

/*--------------------------------------------------------------------*/
/* Insert all statements to be executed at the beginning exclusively */
/* inside the if statement below (loop=0)                             */
/* do not forget that variables which must retain their value from    */
/* one event to the next must be declared in static storage           */
/*--------------------------------------------------------------------*/

  FILE *fp1;
  if(loop == 0){
```

```
    if(flag==1) fp1=fopen("","ab");

    det0=xx[1]*(yy[2]-yy[3])+xx[2]*(yy[3]-yy[1])+xx[3]*(yy[1]-yy[2]);

  HLIMAP(HBOOK_SIZE,name);
/*--------------------------------------------------------------------*/
/* book histograms here do not use labels 1 to 10                     */
/*--------------------------------------------------------------------*/

  for(i=21;i<=29;i++)HBOOK1(i," ph Cherenkov small tanks
",1200.,0.,1200.,0.);
  for(i=31;i<=36;i++)HBOOK1(i," time Cherenkov small
tanks",1200.,0.,1200.,0.);

  HBOOK1(101,"pedestals",10.,0.,10.,0.);
  HBOOK2(102,"t23 vs t21",50.,-500.,500.,50.,-500.,500.,0.);
  HBOOK2(103,"large vs medium",50.,0.,1000.,50.,0.,1000.,0.);
  HBOOK1(104,"time between good pair events",140.,0.,70000.,0.);
  HBOOK1(105,"time between good pair events",100.,0.,6.4,0.);
  for(i=1;i<=6;i++)HBOOK1(110+i,"test ph",100.,0.,100.,0.);
  HBOOK1(107,"large",10.,-.5,9.5,0.);
  HBOOK1(108,"time between triggers good events",140.,0.,70000.,0.);
  HBOOK1(109,"ttotal distribution of short times between
triggers",500.,0.,500000.,0.);
  HBOOK1(110,"ttotal distribution of short times between
triggers",500.,0.,500000.,0.);
  HBOOK1(255,"ttotal distribution of short times between
triggers",500.,0.,500000.,0.);
  for (i=1;i<=3;i++){ HBOOK2(40+i,"ph tube 1 vs
2",50.,0.,1000.,50.,0.,1000.,0.);
  HBOOK1(200+i," time Cherenkov no trigger",500.,0.,500.,0.);
  HBOOK1(203+i," time Cherenkov trigger",500.,0.,500.,0.);
  HBOOK1(230+i,"ph trigger tanks",1000.,0.,1000.,0.);
  }
  for(i=1;i<=6;i++)HBOOK1(210+i," ph trigger pmt",1000.,0.,1000.,0.);
  HBOOK1(221,"phi",72.,-180.,180.,0.);
  HBOOK1(222,"cos theta",100.,0.,1.,0.);
  HBOOK2(223,"ux,uy",40.,-1.,1.,40.,-1.,1.,0.);
  HBOOK1(224,"ux30",100.,-1.,0.,0.);
  HBOOK1(225,"time[3] for east events",400.,0.,800.,0.);
  HBOOK1(226,"time[3] for west events",400.,0.,800.,0.);
  HBOOK1(227,"ttotal distribution of short times between
triggers",200.,0.,200000.,0.);
  HBOOK1(228,"time between triggers",1000.,-1000.,1000.,0.);
  HBOOK1(229,"time between triggers",140.,0.,70000.,0.);
  for(i=1;i<=6;i++)HBOOK1(240+i," ph non-trigger pmt",1000.,0.,1000.,0.);
  HBOOK1(250,"phall for okall=3",1000.,0.,1000.,0.);
  HBOOK1(251,"phpair for okall>=2",1000.,0.,1000.,0.);
  HBOOK1(252," time difference for pair",400.,-200.,200.,0.);
  for(i=1;i<=3;i++)HBOOK1(255+i,"timei-j/2-k/2",400.,-200.,200.,0.);
  for(i=1;i<=3;i++)HBOOK1(260+i," time difference pmts of ok
tanks",600.,-300.,300.,0.);
  for(i=1;i<=3;i++)HBOOK1(263+i," time of ok tanks",900.,0.,900.,0.);
  for(i=1;i<=6;i++)HBOOK1(270+i," pulse difference pmt's of ok
tanks",200.,-10.,10.,0.);
  HBOOK1(309,"ttotal distribution of short times between
triggers",500.,0.,500000.,0.);
  for(i=1;i<=6;i++)HBOOK1(400+i,"pedestals",100.,-20.,80.,0.);
```

```
  for(i=1;i<=3;i++)HBOOK1(420+i,"tank times",140.,0.,700.,0.);
  HBOOK1(430,"trigger tanks",10.,-.5,9.5,0.);
  HBOOK1(440,"scaler bits",30.,-.5,29.5,0.);
  for(i=1;i<=3;i++)HBOOK1(450+i,"phtanks",1200.,0.,1200.,0.);
  for(i=1;i<=3;i++)HBOOK2(460+i,"ph pmt1 vs pmt2
",20.,0.,1200.,20.,0.,1200.,0.);
    }

  loop++;
/*--------------------------------------------------------------------*/
/* Insert all statements to be executed for each individual event    */
/* inside the if statement below (loop>0)                            */
/* However this must be done farther down only once all variables    */
/* have been stored and once pedestals have been calculated          */
/*--------------------------------------------------------------------*/

  if(loop>0)

/*====================================================================*/
/* Store data in the following arrays:                               */
/*    ph[1 to 6]=ADC pulse heights                                   */
/*    time[1 to 6]= TDC values                                       */
/*====================================================================*/

    {
// transfer data from dc_int

ph[1]=data[1];ph[2]=data[3];ph[3]=data[5];ph[4]=data[7];ph[5]=data[9];
ph[6]=data[11];

time[1]=data[25];time[2]=data[26];time[3]=data[27];time[4]=data[28];
time[5]=data[29];time[6]=data[30];

if(loop>=40){scaler[1]=data[41];sctest=scaler[1]-scold;
HF1(228,sctest,1.);HF1(229,scaler[1],1.);scold=scaler[1];
   ttotal=ttotal+scaler[1]/10000.;HF1(109,ttotal,1.);
             bit1=scaler[1];for(i=1;i<=24;i++){bit2=bit1/2;
            if(2*bit2!=bit1)HF1(440,(float)i,1.);bit1=bit2;}
}
// calculate pedestals
      if(loop<30){nped=nped+1;for(i=1;i<=6;i++)ped[i]=ped[i]+ph[i];}

if(loop==30)for(i=1;i<=6;i++){ped[i]=ped[i]/(float)nped;HF1(101,(float)i,
ped[i]);}

  {
     if(loop>40){

       // subtract pedestals and define ok flags. Make plots for ok pmt's

for(i=1;i<=6;i++){satur[i]=0.;if(ph[i]>1050.)satur[i]=1.;ph[i]=ph[i]-
ped[i];ok[i]=0;}

for(i=1;i<=6;i++){if((ph[i]>10.)&&(ph[i]<1200.)&&(ph[anhem[i]]>10.)&&(ph[
anhem[i]]<1200.)&&(time[i]>10.)&&(time[i]<1200.)&&(time[anhem[i]]>10.)&&(
time[anhem[i]]<1200.))ok[i]=1;
```

```
       if(ok[i]==1)
{HF1(20+i,ph[i]/gain[i],1.);HF1(30+i,time[i],1.);HF1(110+i,(float)loop/20
00.,ph[i]);}
       }

       //define tank associated variables
       for(i=1;i<=3;i++){oktank[i]=0;if(ok[2*i]+ok[2*i-
1]==2)oktank[i]=1;ttank[i]=0.;phtank[i]=0.;
       if(oktank[i]==1){ttank[i]=time[2*i-
1]/2.+time[2*i]/2.;phtank[i]=(ph[2*i-1]/gain[2*i-
1]+ph[2*i]/gain[2*i])/2.;
       HF1(26+i,phtank[i],1.);if(satur[2*i]+satur[2*i-
1]!=1)HF1(450+i,phtank[i],1.);HF1(420+i,ttank[i],1.);} }
       okall=oktank[1]+oktank[2]+oktank[3];
       // order tanks according to ph

large=1;if(phtank[2]>phtank[1])large=2;if(phtank[3]>phtank[large])large=3
;

small=1;if(phtank[2]<phtank[1])small=2;if(phtank[3]<phtank[small])small=3
;
      medium=6-small-large;
      phpair=(phtank[large]+phtank[medium])/2.;

       //look at pedestals
       HF1(400+2*small,ph[2*small],1.);HF1(400+2*small-1,ph[2*small-
1],1.);
       //look at events having at least two ok tanks
       if(okall>=2){

      if(phpair>40.){HF1(104,10000.*(ttotal-ttotal2),1.);HF1(105,ttotal-
ttotal2,1.);ttotal2=ttotal;
      HF1(309,ttotal,1.);
        if(flag==1){
        nhung=nhung+1;
        ttnow=ttotal-ttold;
        if(nhung<=goodpairs)
        fprintf(fp1,"%f %f %f %f %f %f %f %f %f %f %f %f %f %f %d\n",
             ph[1],ph[2],ph[3],ph[4],ph[5],ph[6],

time[1],time[2],time[3],time[4],time[5],time[6],scaler[1],ttnow,nhung);
        ttold=ttotal;
        if(nhung==goodpairs){ fclose(fp1);printf("happyend= %d",nhung);}
      }

       HF1(251,phpair,1.);HF1(110,ttotal,1.);HF1(252,ttank[large]-
ttank[medium],1.);}
       //look at which tank triggered and defined the timing of the
trigger (because it was the latest)
       for(i=1;i<=3;i++){trig[i]=0;
       if((oktank[i]==1)&&((time[2*i]>315.&&time[2*i]<325.)||(time[2*i-
1]>315.&&time[2*i-1]<325.)))trig[i]=1;
       if(trig[i]==1)HF1(430,(float)i,1.);}

if(trig[1]+trig[2]+trig[3]==1)HF1(430,(float)(4+trig[1]+2*trig[2]+3*trig[
3]),1.);
       HF1(107,(float)large,1.);
```

```
       for(i=1;i<=3;i++)if(oktank[i]==1){HF1(260+i,time[2*i]-time[2*i-
1],1.);
       HF1(270+i,ph[2*i]/pmean[2*i]-ph[2*i-1]/pmean[2*i-1],1.);
       if(time[2*i]-time[2*i-1]>-100.&&time[2*i]-time[2*i-
1]<100.)HF1(273+i,ph[2*i]/pmean[2*i]-ph[2*i-1]/pmean[2*i-1],1.);
       HF1(263+i,ttank[i],1.); }
       HF2(103,phtank[large],phtank[medium],1.);
       HF2(40+large,ph[2*large-1]/gain[2*large-
1],ph[2*large]/gain[2*large],1.);

       // plot timing of ok tanks that did not trigger
       if(trig[1]+trig[2]+trig[3]==1){ for(i=1;i<=3;i++)

{if(trig[i]==0&&oktank[i]==1)HF1(200+i,ttank[i],1.);if(trig[i]==1&&oktank
[i]==1)HF1(203+i,ttank[i],1.);} }
       // ph spectrum of the trigger pmt and trigger tank

for(i=1;i<=6;i++){if(time[i]>315.&&time[i]<325.&&ok[i]==1)HF1(210+i,ph[i]
,1.);}
       for(i=1;i<=3;i++){if(trig[i]==1)HF1(230+i,phtank[i],1.);}

       // ph spectrum of non-trigger pmt's
       for(i=1;i<=6;i++){if(time[i]<=315.&&ok[i]==1)HF1(240+i,ph[i],1.);}
       phall=(phtank[1]+phtank[2]+phtank[3])/3.;
       if(okall==3){
      HF2(102,ttank[2]-ttank[1],ttank[2]-ttank[3],1.);HF1(250,phall,1.);

if(phall>80.){HF1(255,ttotal,1.);for(i=1;i<=3;i++)HF1(255+i,ttank[i]-
ttank[jj[i]]/2.-ttank[kk[i]]/2.,1.);
      if(ttotal0>0.) HF1(108,10000.*(ttotal-ttotal0),1.);ttotal0=ttotal;
      for(i=1;i<=3;i++)HF2(460+i,ph[2*i],ph[2*i-1],1.);
      alpha=((yy[2]-yy[3])*ttank[1]+(yy[3]-yy[1])*ttank[2]+(yy[1]-
yy[2])*ttank[3])*conv/det0;
      beta=-((xx[2]-xx[3])*ttank[1]+(xx[3]-xx[1])*ttank[2]+(xx[1]-
xx[2])*ttank[3])*conv/det0;
      phi=atan(beta/alpha);if(sin(phi)*beta<0.&&phi>0.)phi=phi-
pi;if(sin(phi)*beta<0.&&phi<0.)phi=phi+pi;
      costh=1.-alpha*alpha-beta*beta;
      if(costh>0.){sinth=pow(1.-costh,.5);costh=pow(costh,.5);
HF1(221,phi*180./pi,1.);HF1(222,costh,1.);
ux=sinth*cos(phi);uy=sinth*sin(phi);HF2(223,ux,uy,1.);ux30=ux*0.866+uy*.5
;HF1(224,ux30,1.);
      if(ux30<-.5) HF1(225,time[3],1.); if(ux30>.5)HF1(226,time[3],1.);
if(ux>.5&&ux<.6&&uy>.7&&uy<.8)HF1(227,ttotal,1.);}
      }
       }}
     }}
    }
}
```